

National Technical University of Athens
School of Rural & Surveying Engineering
Laboratory of Photogrammetry



Εθνικό Μετσόβιο Πολυτεχνείο
Σχολή Αγρονόμων & Τοπογράφων Μηχανικών
Εργαστήριο Φωτογραμμετρίας

GEOMETRIC AND QUALITY COMPARISON OF PRODUCTS DERIVED FROM VERY HIGH RESOLUTION SATELLITE IMAGES

ΓΕΩΜΕΤΡΙΚΗ ΚΑΙ ΠΟΙΟΤΙΚΗ ΣΥΓΚΡΙΣΗ ΚΑΙ ΑΞΙΟΛΟΓΗΣΗ ΠΑΡΑΓΩΓΩΝ ΔΟΡΥΦΟΡΙΚΩΝ ΕΙΚΟΝΩΝ ΠΟΛΥ ΥΨΗΛΗΣ ΑΝΑΛΥΣΗΣ

Postgraduate Diploma Thesis

By
Panagiotis Agrafiotis
Athens, March 2015

Μεταπτυχιακή Εργασία

Παναγιώτης Αγραφιώτης
Αθήνα, Μάρτιος 2015

GEOMETRIC AND QUALITY COMPARISON
OF PRODUCTS DERIVED FROM VERY HIGH
RESOLUTION SATELLITE IMAGES

Postgraduate Diploma Thesis

By
Panagiotis Agrafiotis
Athens, March 2015

ΓΕΩΜΕΤΡΙΚΗ ΚΑΙ ΠΟΙΟΤΙΚΗ ΣΥΓΚΡΙΣΗ ΚΑΙ
ΑΞΙΟΛΟΓΗΣΗ ΠΑΡΑΓΩΓΩΝ ΔΟΡΥΦΟΡΙΚΩΝ ΕΙΚΟΝΩΝ
ΠΟΛΥ ΥΨΗΛΗΣ ΑΝΑΛΥΣΗΣ

Μεταπτυχιακή Εργασία

Παναγιώτης Αγραφιότης
Αθήνα, Μάρτιος 2015

Andreas Georgopoulos
Professor
(Major Professor)

Charalambos Ioannidis
Professor
(Committee Member)

Konstantinos Karantzas
Assistant Professor
(Committee Member)

Acknowledgments

The author would like to thank Astrium GEO-Information Services which provided the Pléiades triplet for research and investigation purposes. In addition, the contribution of NCMA S.A, through the provision of the orthophoto and DSM, produced by aerial photography is acknowledged.

The guidance by Prof. Konstantinos Karantzas and PhD Candidate Aristeidis Vaiopoulos in the field of Panshaperning is also acknowledged.

The offer Maria Teresa Ioannou is acknowledged for providing to me the data and the results of her Diploma Thesis..

Finally, I would like to thank Prof. Andreas Georgopoulos for encouraging me and providing me the opportunity of exploring issues of my choice, always in parallel with his scientific guidance.

Table of Contents

TABLE OF CONTENTS	I
LIST OF FIGURES	III
LIST OF TABLES.....	IV
ABBREVIATIONS	V
ABSTRACT.....	VI
DESCRIPTION OF THE OBJECT	2
Study Area.....	2
PART I.....	4
ACCURACY AND QUALITY COMPARISON OF ORTHORECTIFIED HIGH RESOLUTION SATELLITE IMAGES	4
CHAPTER 1	6
INTRODUCTION.....	6
1.1. State of The Art.....	6
1.2. Test Dataset	7
1.2.1. The Pleiades 1B imagery	8
1.2.2. The GeoEye-1 imagery.....	9
1.2.3. The Aerial orthophoto (LSO)	10
1.3. Control Dataset.....	11
CHAPTER 2	12
METHODOLOGY.....	12
2.1.1. GCP's measurements and Distribution.....	12
2.1.2. Pansharpening.....	13
2.1.3. Image Orientation	14
2.1.4. DSM Extraction and Orthophoto Production	15
CHAPTER 3	16
QUALITY AND ACCURACY ASSESSMENT	16
3.1. Image quality assessment	16
3.1.1. Visual Assessment.....	16
3.1.2. Histogram Based Evaluation	16
3.1.3. Change in Standard Deviation	17
3.2. Spatial Accuracy assessment.....	18
3.2.1. The National Standard for Spatial Data Accuracy (NSSDA).....	19
3.2.2. JRC Guidelines for Best Practice and Quality Checking of Ortho.....	19
3.2.3. The American Society of Photogrammetry and Remote Sensing Standard 19	
3.2.4. Checkpoints Selection and Distribution	20
3.3. Measurements - Results	21

3.4. Conclusion.....	23
PART II.....	25
THE EFFECT OF PANSHARPENING ALGORITHMS ON DIGITAL SURFACE MODEL EXTRACTION AND RESULTING ORTHOIMAGERY	25
CHAPTER 4	27
INTRODUCTION.....	27
CHAPTER 5	29
METHODOLOGY.....	29
5.1. Pansharpening Algorithms	30
5.1.1. Implemented Algorithms and Results	30
5.2. Automatic DSM Generation.....	35
CHAPTER 6	38
ACCURACY ASSESSMENT OF PANSHARPENING ALGORITHMS.....	38
6.1. VLSO and Pleiades 1B PMS-N (IHS-PCA-BROVEY) Accuracy Comparison	38
6.1.1. Four Band Data (RGB and NIR)	38
6.1.2. Three Band Data (RGB)	39
6.2. Pleiades 1B PAN and Pleiades 1B PMS-N (IHS-PCA-BROVEY) Accuracy Comparison	40
6.2.1. Four Band Data (RGB and NIR)	40
6.2.2. Three Band Data (RGB)	41
6.3. Panchromatic Data VS Four Band Data (RGB and NIR) and Three Band Data (RGB)	42
6.3.1. IHS Pansharpening	42
6.3.2. PCA Pansharpening	43
6.3.3. Brovey Pansharpening	44
6.4. Overall Evaluation.....	45
6.5. Concluding Remarks	47
6.6. Future Work	48
REFERENCES.....	50
APPENDIX I	55
APPENDIX II.....	57

List of Figures

Figure 1: The study area, the Antiparos island	2
Figure 2: The normal distribution curve showing a typical bell shape curve (modified from http://theeducatedsociety.com/tag/bell-curve/).	55
Figure 3: Image acquisition from Pleiades 1B satellite (Google Earth preview of the satellite's position).....	8
Figure 4: The acquired image from Pleiades 1B satellite (Google Earth preview of the footprint)	8
Figure 5: Flying elevation, field of regard for 30° nadir angle and revisit time for 53° latitude (Jacobsen, 2011)	9
Figure 6: GeoEye-1 Imagery for the island of Antiparos	10
Figure 7: The Aerial orthophotomosaic (LSO) provided by NCMA S.A.	10
Figure 8: The Aerial orthophotomosaic (VLSO) provided by NCMA S.A.	11
Figure 9: Photogrammetric workflow for Orthoimage Production from stereo imagery	12
Figure 10: Ground control points and checkpoints used for Pleiades 1B data	14
Figure 11: Pleiades 1B orthoimage	15
Figure 12: GeoEye-1 orthoimage produced by (Ioannou and Georgopoulos, 2013)...	15
Figure 13: Examples of visual errors/defects of the orthoimages.....	17
Figure 14: Examples of visual errors/defects of the orthoimages and their histograms	18
Figure 15: Checkpoints distribution on GeoEye-1 orthophoto.....	20
Figure 16: Workflow chart for checking the effects of pansharpening process	29
Figure 17: Basic wavelet based pansharpening (Palsson et al., 2012).....	30
Figure 18: The original MS image (a) and the Pansharpening results from IHS (b), Brovey (c) and PCA (d) algorithms.	31
Figure 19: PCA based Pansharpening.....	32
Figure 20: Standard IHS fusion scheme	33
Figure 21: A zoom of the original MS image (a) and the Pansharpening results from IHS (b), Brovey (c) and PCA (d) algorithms for 4 Bands.	35
Figure 22: DSMs from different pansharpened data.....	36
Figure 23: Graphic representation of Resulting residuals in meters.....	46

List of Tables

Table 1: Examples of the limiting planimetric RMS for the three accuracy standards	20
Table 2: Measured coordinates for GeoEye-1 and Pleiades 1B orthoimagery.	22
Table 3: Resulting residuals of the measured checkpoints	22
Table 4: Bias calculations	22
Table 5: RMSEs and residuals after bias removal	23
Table 6: Measured coordinates for Pleiades 1B orthoimagery created from 4 bands data and compared with the VLISO.	39
Table 7: Resulting residuals of the measured checkpoints	39
Table 8: Measured coordinates for Pleiades 1B orthoimagery created from 3 bands data and compared with the VLISO.	40
Table 9: Resulting residuals of the measured checkpoints	40
Table 10: Measured coordinates for Pleiades 1B orthoimagery created from 4 bands data and compared with the one created using the Panchromatic data.	41
Table 11: Resulting residuals of the measured checkpoints	41
Table 12: Measured coordinates for Pleiades 1B orthoimagery created from 3 bands data and compared with the one created using the Panchromatic data.	42
Table 13: Resulting residuals of the measured checkpoints	42
Table 14: Measured coordinates for Pleiades 1B orthoimagery created from Panchromatic data compared with measured coordinates on orthoimagery produced from 3band data (RGB) and 4 band data (RGB-NIR) created with IHS Pansharpening method.	43
Table 15: Resulting residuals of the measured checkpoints	43
Table 16: Measured coordinates for Pleiades 1B orthoimagery created from Panchromatic data compared with measured coordinates on orthoimagery produced from 3band data (RGB) and 4 band data (RGB-NIR) created with PCA Pansharpening method.	44
Table 17: Resulting residuals of the measured checkpoints	44
Table 18: Measured coordinates for Pleiades 1B orthoimagery created from Panchromatic data compared with measured coordinates on orthoimagery produced from 3band data (RGB) and 4 band data (RGB-NIR) created with Brovey Pansharpening method.	45
Table 19: Resulting residuals of the measured checkpoints	45
Table 20: Resulting residuals for all performed tests for Pleiades 1B dataset.	46

Abbreviations

3D	Three Dimensional
CCD	Charge coupled device (Image Sensors)
CMOS	Complementary metal oxide semiconductor
CP	Control Point
DOQ	Digital Orthophoto Quadrangles
DSM	Digital Surface Model
GCP	Ground Control Point
GE1	GeoEye-1 satellite
GPS	Global Positioning System
GSD	Ground Sample Distance
HCS	Hyperspherical Colour Space
HiRI	High resolution optical imager
IHS	Intensity Hue Saturation
LSO	Large Scale Orthophotos
MS	Multi-Spectral
MTF	Modulation Transfer Function
NIR	Near Infrared
PAN	Panchromatic
PCA	Principal Components Analysis
RGB	Red-Blue-Green
RMSE	Root Mean Square Error
RPC	Rational Polynomial Coefficient
VHR	Very High Resolution
VLSO	Very Large Scale Orthophotos
WV2	World View 2 satellite

Abstract

This study aims to assess the accuracy and radiometric quality of orthorectified high resolution satellite imagery from Pleiades-1B satellites through a comparative evaluation of their quantitative and qualitative properties. In addition, the effect of pansharpener algorithms on Digital Surface Model (DSM) Extraction and consequently on the resulting Orthoimagery is investigated.

A Pleiades-B1 stereopair of high resolution images taken in 2013, two adjacent GeoEye-1 stereopairs from 2011 and aerial orthophotomosaic (LSO) provided by NCMA S.A (Hellenic Cadastre) from 2007 with a GSD of 0.50m have been used for the comparison tests. As control dataset the orthophotomosaic from aerial imagery provided also by NCMA S.A (0.25m GSD) from 2012 was selected. The process for DSM and orthoimage production was performed using commercial digital photogrammetric workstations.

The two resulting orthoimages from Pleiades 1B and GeoEye-1 data, the Orthoimagery from the Pleiades 1B pansharpener data and the aerial orthomosaic (LSO) are relatively and absolutely evaluated for their quantitative properties. Test measurements are performed using the same check points in order to establish their accuracy both as far as the single point coordinates as well as their distances is concerned. Check points were distributed according to JRC Guidelines for Best Practice and Quality Checking of Ortho Imagery, and NSSDA standards while areas with different terrain relief and land cover were also included. The tests performed are based also on JRC, ASPRS and NSSDA accuracy standards. Finally, tests were carried out in order to assess the radiometric quality of the orthoimagery.

The results are presented with a statistical analysis and they are evaluated in order to present the merits and demerits of the imaging sensors involved for orthoimage production and the effects of pansharpener algorithms on the Orthoimagery of Pleiades 1B satellite. The results also serve for a critical approach for the usability and cost efficiency of satellite imagery for the production of Large Scale Orthophotos.

Description of the Object

As satellite optical sensor technology progresses, very high resolution (VHR) images from space become available and lucrative for large scale mapping. Resolutions of less than 1m reaching the level of a few tens of centimetres are common today thus enabling the users to distinguish fine detail on the earth's surface, like buildings, individual trees and even smaller objects. For applications concerned with mapping, cadastral recording and land monitoring VHR satellite imagery is directly rivalling conventional or even digital aerial images of comparable resolution. The Pléiades 1B are a very high-resolution satellite constellation delivering 50-cm Ortho products as a standard. In the context of the Pleiades evaluation program, the Laboratory of Photogrammetry of National Technical University of Athens acquired a triplet of high resolution images taken in 2013 by Pleiades 1B over the small Cyclades island of Antiparos in order to assess their usability and accuracy and compare it to similar satellite sensors.

This thesis aims to report the assessment of the accuracy and radiometric quality of orthorectified high resolution satellite imagery from Pleiades-1B satellites through a comparative evaluation of their quantitative and qualitative properties. In addition, the advantages and limits of the Pleiades Imaging for producing Large Scale Orthophotos (LSO) are investigated. Moreover, in Part II, this study investigates the geometric effects of pansharpening algorithms on automatically generated DSMs and thus on the resulting Orthoimagery through a comparative assessment of their geometric accuracy using only the Pleiades 1B data.

Study Area

The study area, the small Cyclades island of Antiparos has an area of 35 km².

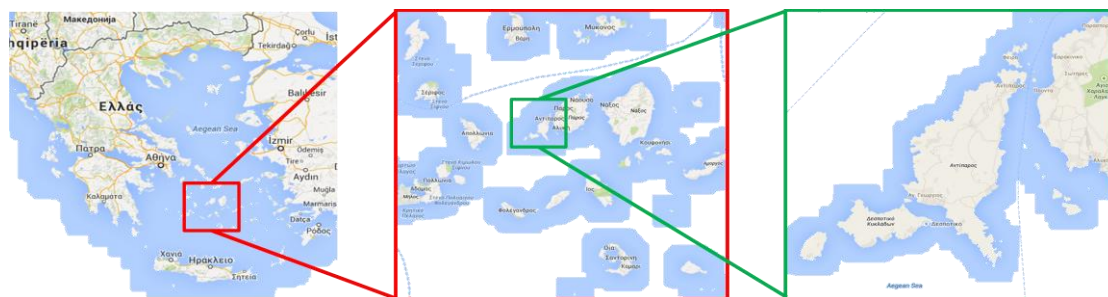


Figure 1: The study area, the Antiparos island

It measures 12.5 kilometres long and 5.5 km wide and a coastal perimeter of 54 km. Even though the island is almost flat, a few little hills in the centre reach a maximum elevation of 300 metres. The landscape is rather wild and varied including a main settlement and agricultural fields. Finally, on the west coast there are sheer cliffs.

Part I

Accuracy and Quality Comparison of Orthorectified High Resolution Satellite Images

CHAPTER 1

Introduction

This chapter aims to report on the assessment of the accuracy and radiometric quality of orthorectified high resolution satellite imagery from Pleiades-1B satellites through a comparative evaluation of their quantitative and qualitative properties. In addition, the advantages and limits of the Pleiades Imaging for producing Large Scale Orthophotos (LSO) are investigated.

1.1. State of The Art

In the literature, the radiometric characteristics and the geometric accuracy of optical sensors and their resulting imagery have been extensively addressed in various contributions.

In order to evaluate the geometric accuracy of ground points from integrated Global Positioning System (GPS), inertial navigation system (INS), and high-resolution linear array CCD sensor data, Zhou and Li (Zhou and Li, 2000) present the experimental results on the attainable accuracy of ground points versus the number and the distribution of ground control points (GCPs), versus the image measurement error of GCPs and checkpoints, and versus the order of the polynomial fit to the orbital path. To this direction, they establish a geodetic control network which is used for testing the 3D accuracy of the simulated new generation IKONOS high-resolution satellite imagery.

Greenfeld (Greenfeld, 2001) evaluates a Digital Orthophoto Quadrangle (DOQ) using the NSSDA standards in order to establish the positional accuracy of the data. The DOQ was also evaluated for its geometric, radiometric, and mosaicking accuracies. Finally, the appropriateness of DOQs in the context of a parcel-based GIS was addressed.

In Eisenbeiss et al., (2004) the processing of IKONOS and QUICKBIRD imagery of two different datasets is described for analyzing the geometric accuracy potential of these images for 3D point positioning, orthoimage and DSM generation. GCPs with an accuracy of 0.2-0.4 m have been used in both sites and the investigations for 3D point positioning included 4 different sensor models, different GCPs measurement, variable number of control points and area covered by them. The results showed that the Rational Polynomial Coefficient (RPC) model compared to 2D and 3D affine models are more general and can model sufficiently imaging modes that depart from linearity.

Niu et al., 2004 present the geometric modeling principles and photogrammetric processing methods involved in high-precision mapping using stereo IKONOS and QuickBird images. After a description of the imaging geometry and the systematic errors in the Rational Function-based sensor model, the results of a comparison study of IKONOS and QuickBird geopositioning accuracy improvement in which different adjustment models, as well as different number and configuration of ground control points, are presented.

In the work of Ioannidis and Katsigiannis (Ioannidis and Katsigiannis, 2006) the impact of using various models is studied for the determination of orientation parameters or georeferencing of high resolution satellite images, on the accuracy of the extracted DSM and orthorectified images. To achieve that, empirical and physically based models are investigated (i.e. Rational Functions (RFC), orbital parameter model etc.), and applied on a pair of IKONOS stereo Geo product images. Twenty three ground points were measured by GPS, scattered all over the area covered by the images. The quality control was made by optical inspection while accuracy controls included the calculation and statistical analysis of the deviations of the measured on the orthoimages coordinates from the known accurate coordinates of the 14 check points. Also, accuracy controls were made between the ortho-images, which were produced from PCI and LPS, using various combinations of GCPs.

The study published in (Aguilar et al., 2008) presents the assessment of different sensor models in order to achieve the best geometric accuracy in orthorectified imagery products obtained from IKONOS Geo Ortho Kit and QuickBird basic imagery. The final orthoimages are compared, both geometrically and visually, with the panchromatic orthophotos based also on a photogrammetric flight with an approximate scale of 1:20000. Two-dimensional root mean square errors (RMSE 2D) in independent check points are used as accuracy indicators.

Finally, Crespi and De Vendictis (2009) evaluate data products generated from High Resolution Satellite Imagery (HRSI) in order to verify if their quality fits the desired features and, if necessary, to obtain the image correction parameters to be used at the ground processing centre. Nevertheless, it is often useful to have tools to evaluate image quality also at the final user level. Image quality is described by the Modulation Transfer Function (MTF). Tests were performed on high resolution imagery acquired by the QuickBird, WorldView-1 and Cartosat-1 satellites.

However, these contributions do not perform any comparative evaluation on the quantitative and qualitative properties of the resulting orthoimagery exploiting aerial Large Scale Orthophotos and Very Large Scale Orthophotos. In addition, the aforementioned studies do not evaluate data captured by Pleiades 1B satellite.

1.2. Test Dataset

A Pleiades 1B stereopair of high resolution images taken in 2013 (0.50m GSD), two adjacent GeoEye-1 stereopairs (0.50m GSD) acquired for a diploma thesis in 2011 from which a high resolution orthophoto had already been produced and aerial LSO (0.50m GSD) provided by the Hellenic National Cadastre & Mapping Agency S.A. (NCMA S.A) from 2007 have been used for the comparison tests.

1.2.1. The Pleiades 1B imagery

The Pléiades twins are very high-resolution satellites delivering 50cm Ortho products as a standard. Pleiades-1B satellite sensor was successfully launched on December 2, 2012. Built by AIRBUS Defence & Space, the satellite was launched from a Soyuz launcher at the European Space Centre in French Guiana. Pleiades-1A and 1B satellites will be phased 180° apart in the same near-polar sun-synchronous orbit at an altitude of 694 km, enabling daily revisits to any location on the planet. The sensor can reach a ground resolution of 0.7m in panchromatic mode and 2.8m in multi-spectral mode in vertical direction.



Figure 2: Image acquisition from Pleiades 1B satellite (Google Earth preview of the satellite's position)

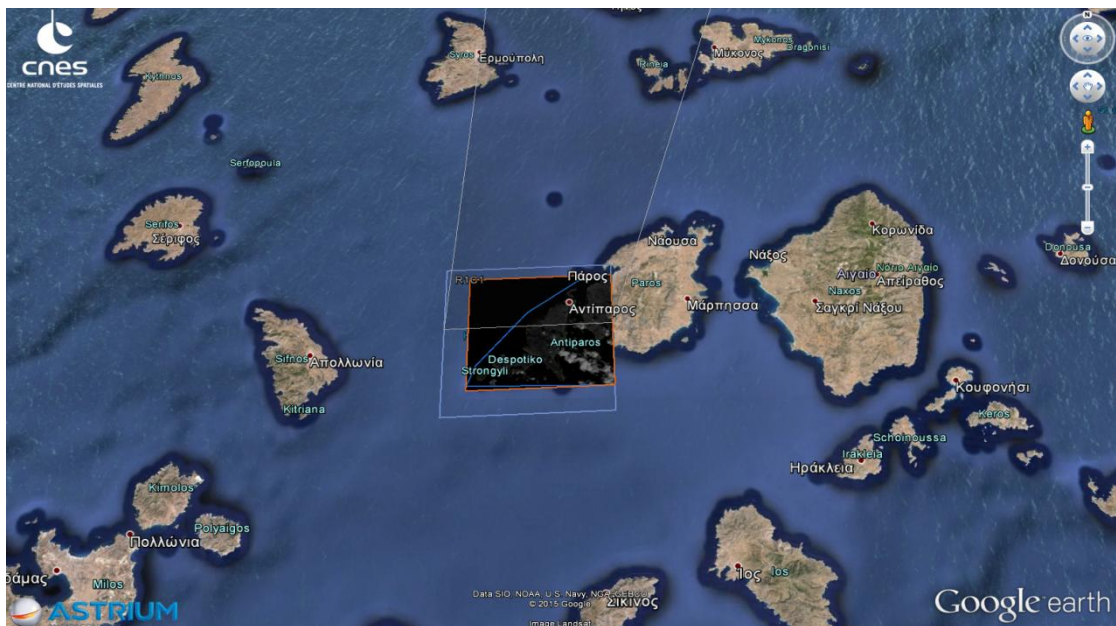


Figure 3: The acquired image from Pleiades 1B satellite (Google Earth preview of the footprint)

The images provided for this work were acquired in the tri-stereo mode for 3D information. According to this acquisition scheme, the satellite rotates around its axis and the HiRI camera scans a target area from three different viewing directions during one pass, thus resulting in a triplet (Gleyzes et al., 2012).

However, for reasons of objectivity in comparison with data from GeoEye-1, only the 2 external images of the tri-stereo were used. The images were acquired on 9th April 2013 in the morning within 22.5 seconds interval. The average viewing angles of the two selected images are, respectively, 6.30° and 9.47° in across-track direction with respect to the nadir and 1.63° and -12.39° in across-track direction.

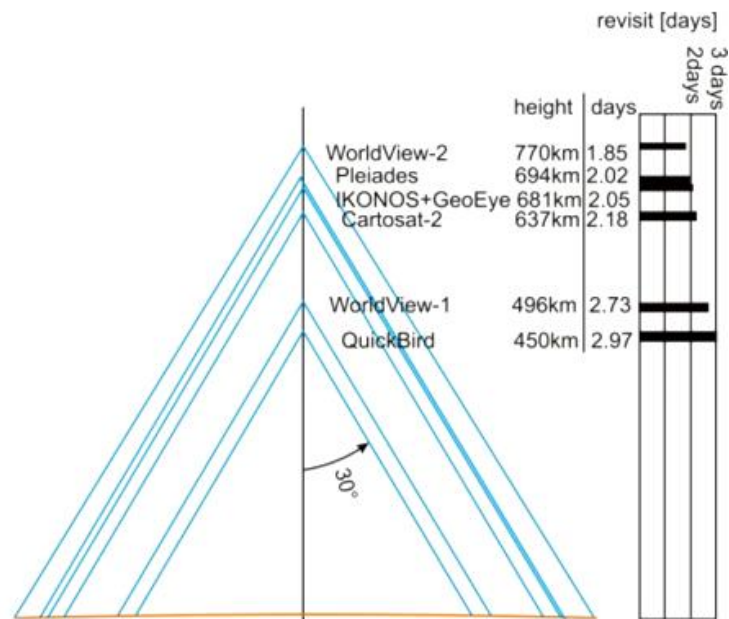


Figure 4: Flying elevation, field of regard for 30° nadir angle and revisit time for 53° latitude (Jacobsen, 2011)

With comparison to GE1 and WV2, Pléiades offers larger field of view and acquisition capability at similar ground resolution (Figure 5). One interesting aspect of the Pléiades constellation is the acquisition mode, which can be target collection, single-pass strip mapping, stereo and tri-stereo and corridor acquisition.

1.2.2. The GeoEye-1 imagery

Geoeye-1 satellite was launched in September 2008. The sensor's vertical ground resolution of 0.41m for panchromatic imagery and 1.65 m for the 4-band multispectral imagery is resampled to 0.50 m and 2.00 m, respectively for commercial customers. The Geoeye-1 sensor was designed mainly for commercial use, with Google as one of its most valued customers. Google uses the imagery for their Google Maps and Google Earth applications. Geoeye Inc. markets this imagery by offering three basic product packages, which are distinguished by the level of positional accuracy they produce.

For the purposes of this study, two adjacent Geoeye-1 stereopairs from December 2011 were used. They are accompanied by an RPC camera model file for georeferencing.



Figure 5: GeoEye-1 Imagery for the island of Antiparos

In all datasets the stereo images offer along-track stereoscopy. In fact Pleiades 1B and GeoEye-1 satellites belong to the last generation agile satellite systems, able to rotate on their axis and acquire stereo images along-track on the same orbit. As a result of this acquisition mode, the time difference between the two stereo images composing a stereo pair is in the range of seconds or minutes. This advantage of a small time interval is that the sun illumination conditions are almost constant and changes in the scene are limited to moving objects, like boats.

1.2.3. The Aerial orthophoto (LSO)

The tested LSO provided by NCMA S.A had 0.50m GSD and the imagery was taken on 2007. This dataset has a geometric accuracy of $RMSE_{XY} \leq 1.41m$ (95% confidence level) and the dimensions of the final 24-bit orthoimages are 4000 x 3000 pixels.

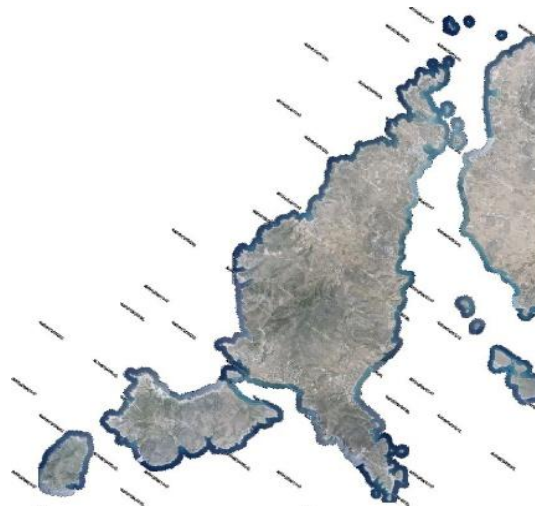


Figure 6: The Aerial orthophotomosaic (LSO) provided by NCMA S.A.

The DEM used for producing these orthophotos was in raster format having a 5 meters pixel size on the ground. The dimension of these raster files was 4600 x 3600 pixels and they had an overlap of 300 meters or 60 pixels.

1.3. Control Dataset

In order to evaluate the produced orthoimages, accuracy specifications had to be set as a reference for the purpose of inferring about the actual metric efficiency of the product. As control dataset the aerial imagery orthomosaic (VLSO) provided by Hellenic National Cadastre & Mapping Agency S.A. (NCMA S.A) was used. It had 0.25m GSD and the imagery was taken on August 12th 2012. According to NCMA S.A the orthomosaic of the control dataset was created from aerial imagery at acquisition scale of 1:15000 using a ZEISS RMK TOP 30 camera having a lens of 153.12mm. According to the NCMA S.A., the acquired images were scanned at 1700 dpi (1pixel = 15 μ m). As the LSO, the digital files of the VLSO, was in JPEG 2000 format, containing also the georeference in a JPW file. These files are of 2000 x 1500 meters on the ground or 8000 x 6000 pixels. To produce this orthoimagery, a DSM was created having 5m grid interval.

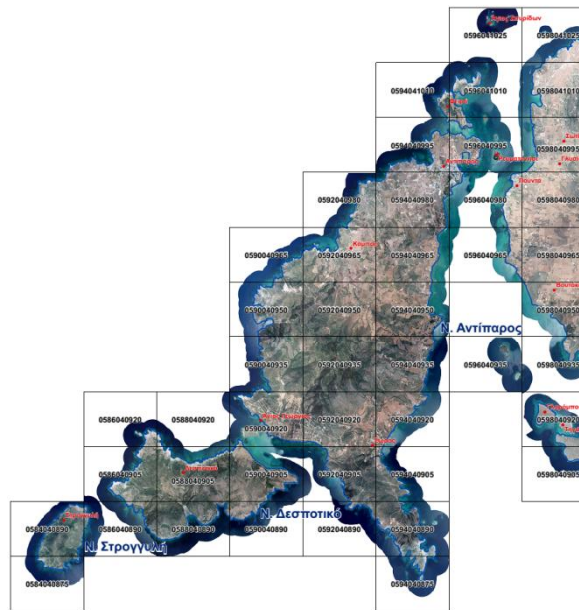


Figure 7: The Aerial orthophotomosaic (VLSO) provided by NCMA S.A.

CHAPTER 2

Methodology

In this work the classical photogrammetric workflow was followed available in ERDAS Photogrammetry Tool (former LPS) environment (ERDAS 2014) for the processing of the stereo satellite imagery, DSM generation and orthorectification (Figure 9).

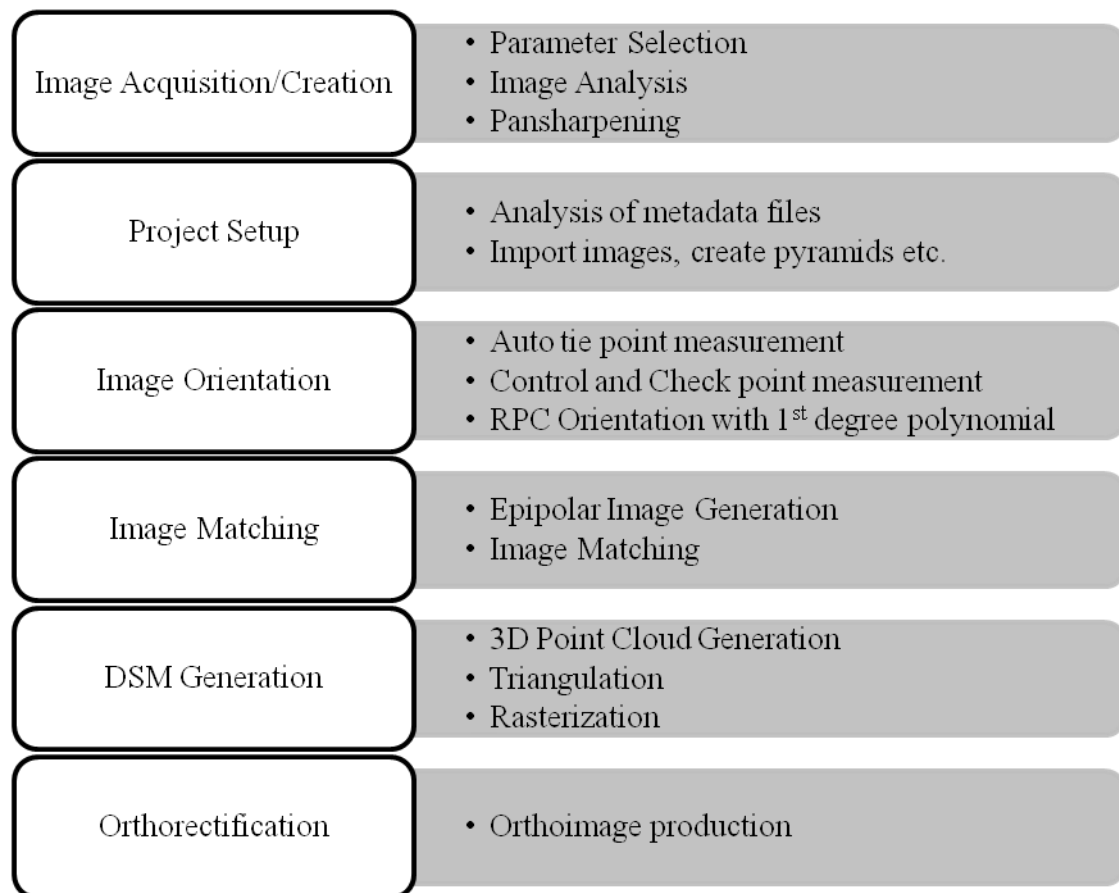


Figure 8: Photogrammetric workflow for Orthoimage Production from stereo imagery

2.1.1. GCP's measurements and Distribution

A number of ground control points were determined by GPS observations for a previous work (Ioannou and Georgopoulos, 2013), which were suitably post-processed in order to get accurate measurements (mean uncertainty of 0.010m),

distributed all over the area of interest. Some of these points have been used for the determination of orientation parameters as GCPs, and the rest as check points.

2.1.2. Pansharpening

Pre-processing the Geoeye-1 and Pleiades 1B image products is a necessary stage before the commencement of the photogrammetric procedures involved in producing the orthophoto. The three stereopairs, 2 from GeoEye-1 which contain the northern and southern regions of the island of Antiparos and one from Pleiades 1B containing the whole island, included 5 bands; one panchromatic with a GSD of 0.50 m and four multispectral (R, B, G and NIR) with a GSD of 2.00 m. For this study, only the three multispectral bands Red, Green and Blue were necessary.

Thus, pansharpening procedures took place in order to enable the subsequent photogrammetric processing of the imagery. Various algorithms were tested in order to achieve the optimal visual result, including the Principal Component Analysis technique, the IHS (Intensity-Hue-Saturation), the Brovey fusion and the HCS (Hyperspherical Color Space) Resolution Merge. From these tests, the algorithm HCS Resolution Merge proved to yield the most visually acceptable results for the available Geoeye-1 stereo pairs and the algorithms IHS for Pleiades 1B stereopair. More details about the evaluation of the aforementioned pansharpening algorithms in terms of geometric accuracy are presented in Part II.

2.1.2.1 IHS for Pleiades 1B Data

A high-resolution colorized product from Pleiades 1B data was produced by using the IHS pan-sharpening algorithm. The Intensity-Hue-Saturation (IHS) method (Haydn et al., 1982) has been widely used (Carper et al., 1990, Chavez and J. Bowell, 1988, Edwards and P. Davis 1994, Tu et al., 2004) for pansharpening satellite images. In this frequently used method, a component derived from the MS image is substituted for a component derived from the PAN image and then the fused or pansharpened image is obtained from the inverse transformation. The basic idea is to first transform the MS image into intensity (I), hue (H) and saturation (S) components (IHS colour space). The next step is to adjust the Pan image so that it has the same mean and variance as the intensity component of the MS image. The intensity component is then replaced with the appropriately scaled Pan image and finally the inverse IHS transformation is taken to get the fused image. The IHS method produces images that have high spatial resolution and low spectral quality (Palsson et al., 2012).

2.1.2.2 HCS for GeoEye-1 Data

Hyperspherical Color Space (HCS) pan-sharpening (Padwick et al, 2010) is an algorithm especially designed for processing images captured by the Worldview-2 satellite, which supports an 8 band multispectral and panchromatic sensor. The main concept of the algorithm is a transformation from the local color space to the hyperspherical color space. The multispectral RGB data are redefined by its band components into angular variables (ϕ_1 , ϕ_2 , ϕ_3) which describe the color or hue, and a radial component (I) which defines the intensity of the color in hyperspherical space. The naïve approach of the algorithm simply replaces the multispectral intensity component with an intensity matched version of the panchromatic band using the normalized mean and standard deviation of the hyperspherical data. This is followed

by a reverse transformation into the RGB color space for the compilation of the pan-sharpened image (Padwick et al, 2010). The technique is applicable to images composed of at least three bands and ideal for those with a great number of bands, such as Worldview-2, but the results were more than satisfactory for the Geoeye-1 RGB image of this project.

2.1.3. Image Orientation

The orientation of the images was performed using the commercial software ERDAS Imagine Photogrammetry Toolbox 2014. After importing the images with their RPC and metadata information and generating the pyramids, automatic tie point measurement and inspection of their positions took place in order to ensure the relative orientation between the two images of the stereo pair. The aim was to link the images and get a stable block. In total 64 points for Pleiades 1B project and 50 points for GeoEye-1 project were measured.

The rigorous photogrammetric processing for the orientation of the images require ground control information to orient the block in a given absolute ground system. Subsequently, ground control points (GCPs) were measured on the images and a 1st degree polynomial RPC refinement was performed. 4 GCPs and 6 checkpoints were used for Pleiades 1B data achieving a RMSE of 0.045m while 5 GCPs and 10 checkpoints were used for GeoEye-1 data achieving a RMSE of 0.160m. The occurred deviation between the RMSE of Pleiades 1B and GeoEye-1 data is justified by the increased radiometric saturation of GeoEye-1 imagery and is discussed further in 3.1.1. At this point it is noted that on the Pleiades 1B data less GCPs and checkpoints were measured because of the clouds on the lower right corner of the imagery.

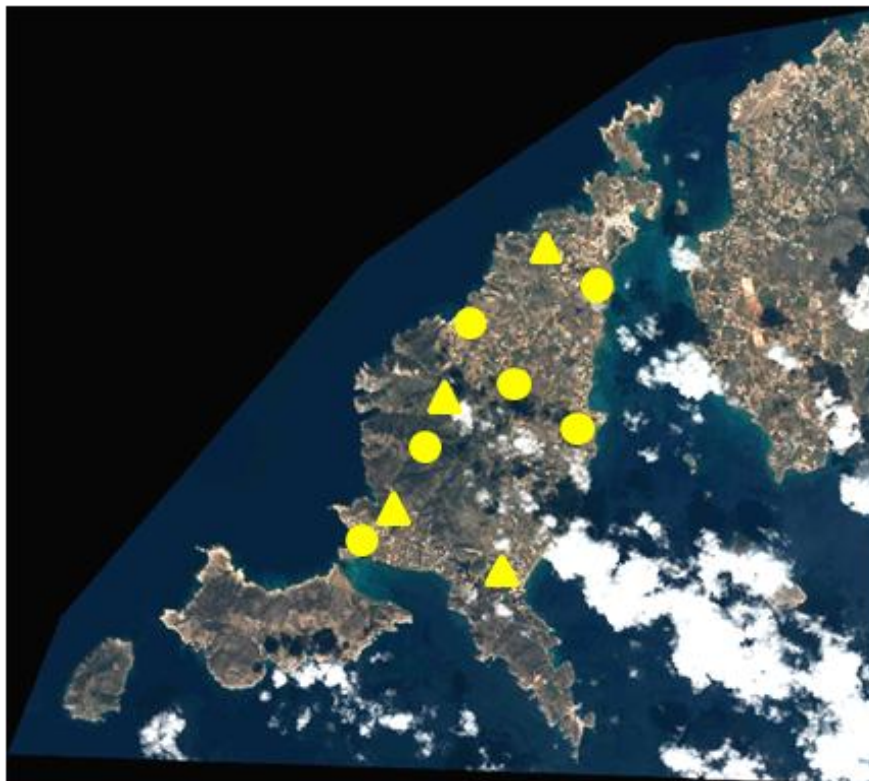


Figure 9: Ground control points and checkpoints used for Pleiades 1B data

2.1.4. DSM Extraction and Orthophoto Production

For the DSM extraction, an automatic procedure was applied for Pleiades 1B while a semi-automatic one was applied for the GeoEye-1 stereopair. The semi-automatic procedure was implemented because of problems occurring on coastal and rocky areas presenting steep terrain. In addition, GCPs were used for transferring the scale and real elevation values while the grid interval was selected at 10m. As regards the production of the orthoimages, they were created using bilinear interpolation. A GSD of 0.50m was selected while it should be mentioned that the orthorectification of all images of the stereopairs was performed in order to check the DSM for gross errors by subtracting them. Finally, it was decided to use the most nadir images for the orthophoto production.



Figure 10: Pleiades 1B orthoimage



Figure 11: GeoEye-1 orthoimage produced by (Ioannou and Georgopoulos, 2013)

CHAPTER 3

Quality and Accuracy Assessment

The results are presented with a statistical analysis and they are evaluated in order to present the merits and demerits of the imaging sensors involved. To this direction the Standard Deviation (σ) or sigma is computed as an indicator of how well the measurements fit to each other and as a measure of precision. In addition, the Root Mean Square Error (RMSE) is computed for Northing and Easting coordinates. As observed, in aerial LSO and Geoeye-1 orthoimage, the Standard Deviation and $RMSE_{X,Y}$ differ, indicating a systematic error in Y axis. Thus, a bias removal procedure was applied in order to evaluate orthoimages objectively and accurately. The produced orthophotos were assessed for a final scale of 1:5000.

3.1. Image quality assessment

The radiometry of an image is satisfactory when the relationship between the ground reflectance of the target and the grey level of the pixel on the image is correct (Crespi and De Vendictis, 2009). Pleiades 1B and GeoEye-1 sensors provide images with radiometric resolution of 12 bit/pixel and 11 bit/pixel respectively. Thus, a higher dynamic range and signal-to-noise ratio with respect to traditional scanned 8-bit/pixel images is expected (Poli et al., 2014).

3.1.1. Visual Assessment

Visual inspection of the orthoimages was applied in order to identify errors and/or image defects. Only a subset of the data is shown in order to display more detail. As an example, in GeoEye-1 images some abrupt changes of brightness and contrast were observed. In addition, many regions presented extremely dark/light tones, i.e. high contrast, predominantly on the buildings and along the roads. Contrary, in Pleiades 1B image, the radiometric saturation of certain regions is especially prominent presenting much more information and clearer forms. Moreover, the orthoimages resulting from Pleiades 1B imagery are much darker than the LSO and Geoeye-1 imagery. Important radiometric changes between two or more images are critical during automatic homologue point identification and during image correlation thus causing mismatches and wrong height estimation (Poli et al., 2014).

3.1.2. Histogram Based Evaluation

Histograms are the basis for numerous image processing techniques. In addition, histograms provide useful image statistics. In a dark image, the components of the histogram are concentrated on the low side of the intensity scale while these

components of a light image are biased toward the high side of the scale. The histogram of a low contrast image has a limited range while on a high contrast image the components of the histogram cover a wide range of the intensity scale (Gonzalez and Woods, 2008).

3.1.2.1 Relative Shift in the Mean

The mean value of the pixels in a band is the central value of the distribution of the pixels in that band. The relative shift in the mean value quantifies the changes in the histogram of the image due to processing.

3.1.3. Change in Standard Deviation

The standard deviation gives information about the spread of the histogram. The change in the standard deviation of the distribution is considered in addition to the shift in the mean. A combination of these two metrics quantifies the changes in the shape of the histogram of each band. The histograms of the images are shown in Figure 14. The mean value, the median and the standard deviation are also plotted. The histogram is spread over a large range of pixel Digital Number values if the standard deviation is high. The relative shift in the mean and standard deviation help to visualize the change in the gray level distribution of the image bands.

In figure 13, histograms of the presented part of the study area, indicates that LSO orthoimagery is characterized by low contrast and high luminosity. However, GeoEye-1 orthoimagery presents higher luminosity than LSO orthoimage and very high frequency of tones near the white (255). Pleiades 1B orthoimagery presents a more normalized histogram with a wide range and components concentrated near the lower side of the scale, indicating a darker image.

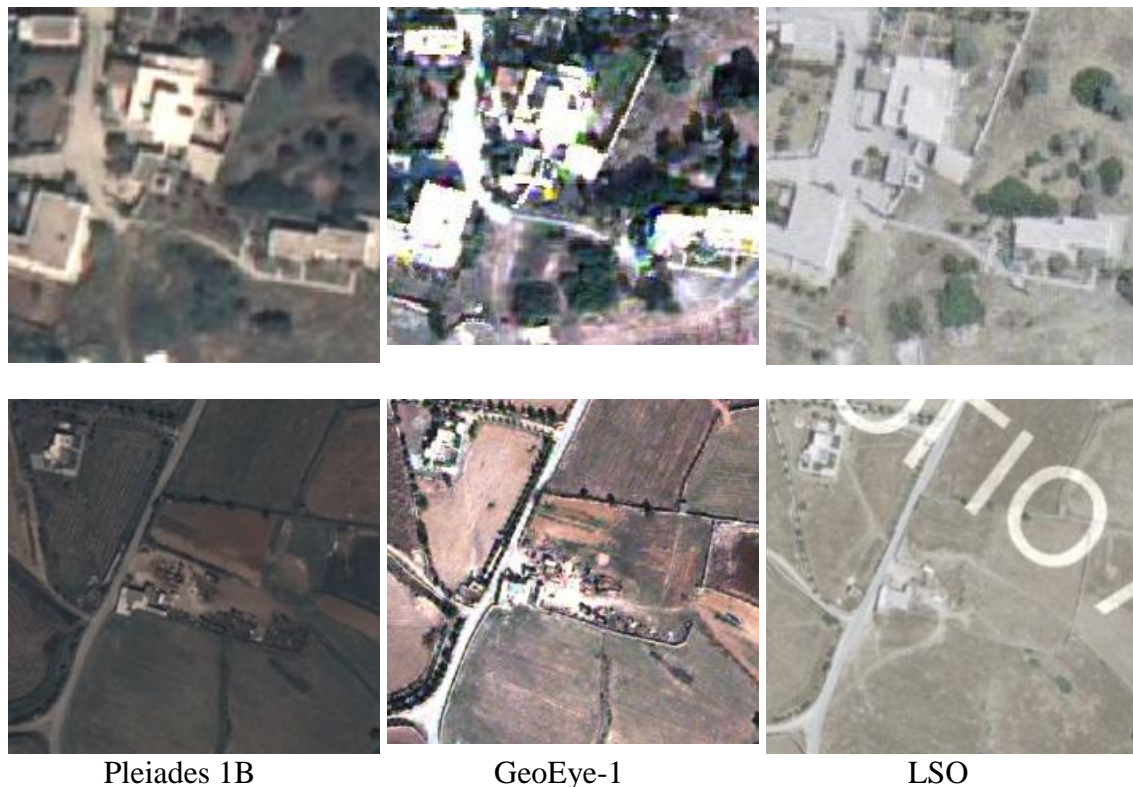


Figure 12: Examples of visual errors/defects of the orthoimages

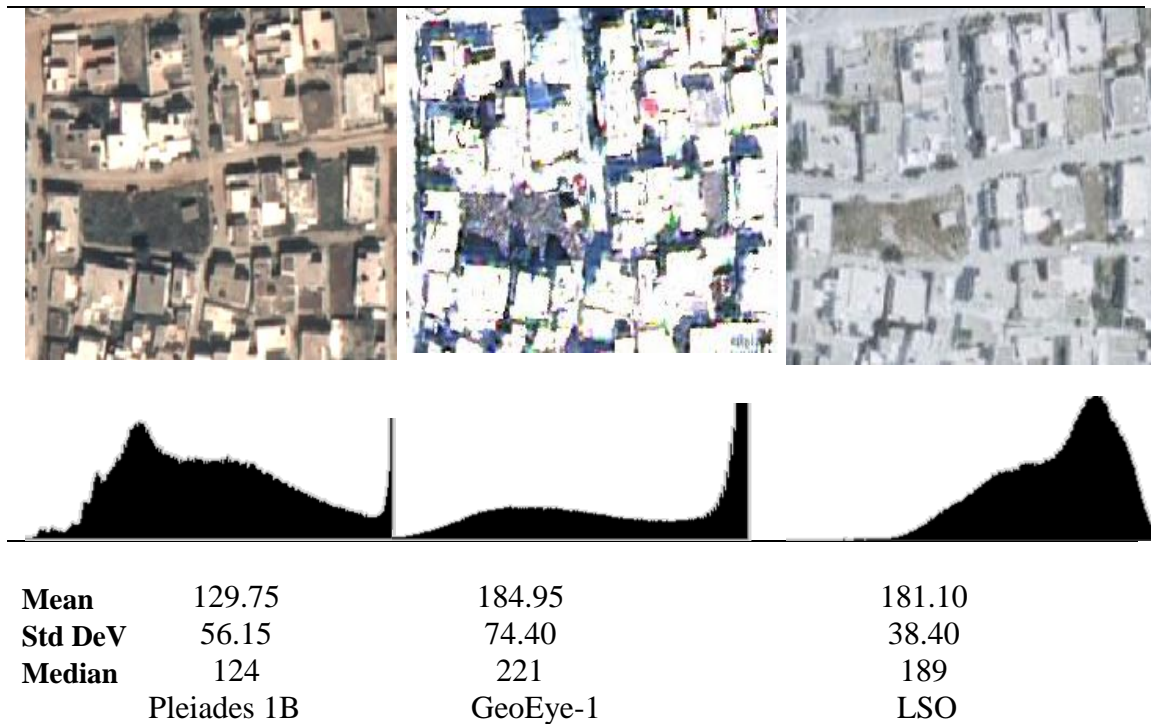


Figure 13: Examples of visual errors/defects of the orthoimages and their histograms

In addition to visual inspection of the images, the noise level and the geometrical resolution and sharpness which is described by the Modulation Transfer Function (MTF) are encountered in the literature. By the term noise the non-homogeneities in the image are described and it is evaluated on non-homogeneous areas. Over these areas, the noise variation is considered as function of intensity. It should be noted that noise for CCD-images is not additive but intensity-dependent (Poli et al., 2014). The Modulation Transfer Function (MTF) is used to estimate the spatial performance of an imaging sensor. In case of on-orbit MTF estimation, the edge method is generally used (Helder and Choi, 2003; Kohm, 2004; Leger et al., 2004; Crespi and De Vendictis, 2009, Poli et al., 2014).

3.2. Spatial Accuracy assessment

The two resulting orthoimages and the aerial imagery orthophoto (LSO) were evaluated relatively and absolutely for their quantitative and qualitative properties. Check points were measured on the VLSO product and test measurements were performed using the same check points in order to establish their accuracy both as far as the single point coordinates as well as their distances were concerned. 26 Check Points for Pleiades 1B and 26 Check Points for Geoeye-1 and LSO were distributed in total according to JRC Guidelines for Best Practice and Quality Checking of Ortho Imagery (Kapnias et al., 2008) and National Standard for Spatial Data Accuracy (NSSDA) (FGDC, 1998) standards while areas with different terrain relief and land cover were also included. Performed tests were also based on JRC, ASPRS and NSSDA accuracy standards.

3.2.1. The National Standard for Spatial Data Accuracy (NSSDA)

The NSSDA implements a statistical and testing methodology for estimating the positional accuracy of points on maps and in digital geospatial data, with respect to georeferenced ground positions of higher accuracy. The NSSDA applies to georeferenced maps and digital geospatial data, in either raster, point, or vector format (FGDC, 1998). The NSSDA does not determine pass/fail criteria which is left to the users i.e. does not define threshold accuracy values and uses the root-mean-square error (RMSE) to estimate positional accuracy. The standard provides the following equation which is based on a 95 percent confidence level to determine the horizontal accuracy of the data without giving any specifics to the absolute value.

$$NSSDA_h = 2.447 \times RMSE_x = 2.447 \times RMSE_y \text{ (if } RMSE_x \neq RMSE_y)$$

or

$$NSSDA_h = 1.73 \times RMSE_r \text{ (if } RMSE_x = RMSE_y), \text{ where } RMSE_r = \sqrt{(RMSE_x)^2 + (RMSE_y)^2}$$

3.2.2. JRC Guidelines for Best Practice and Quality Checking of Ortho

These guidelines apply to digital orthoimagery products, generated from either film cameras or digital sensors, on both airborne or satellite platforms for the scope of applications requiring accuracy of 0.5m-10m pixel size and large scale mapping or cadastre applications (0.5m or better). All stages of the production chain affecting geometric accuracy and radiometric quality of the final product are considered (Kapnias et al., 2008). As with the NSSDA procedure, the final orthoimage is assessed using the RMSE_x and RMSE_y and the associated DSM from RMSE_z. The use of RMSE provides a straight forward global statistic for assessing the final geometric accuracy. Additional indexes such as the mean error and the error standard deviation can be used in order to better describe the spatial variation of errors or to identify potential systematic discrepancies.

3.2.2.1 N.C.M.A. S.A. (Hellenic Cadastre) Guidelines

Based on the aforementioned JRC Guidelines, the Hellenic Cadastre was specialized them for checking the accuracy of the produced LSO. The check point horizontal accuracy set by N.C.M.A. S.A. for the evaluation of its orthophotos of scale 1:5000 is as follows:

$$RMSE_{XY} \leq 1.41 \text{ m, } RMSE_x \leq 1.00 \text{ m and } RMSE_y \leq 1.00 \text{ m,}$$

Absolute accuracy of ≤ 2.44 m for a 95% level of confidence

3.2.3. The American Society of Photogrammetry and Remote Sensing Standard

This standard, which was first approved by the ASPRS Professional Practice Division in March 1990, is the first to deal with large-scale topographic and engineering-grade maps. The major feature of the standard is that it indicates accuracy at ground scales versus a published paper map scale. Thus, digital spatial data of known ground scale accuracy can be related to the appropriate map scale for graphic presentation. The ASPRS standard defines the accuracy as limiting Root Mean Squares (RMS) errors in terms of the project's survey coordinates for checkpoints as determined by the ground scale of the map. The standard also provides three sets of accuracy figures for maps produced with different accuracy levels. According to the standard, a map with the highest accuracy is called a "Class 1" map, while a map produced within limiting

RMS errors of twice or three times those allowed for a Class 1 map are to be designated as Class 2 or Class 3 maps, respectively. The ASPRS standard defines the accuracy as limiting Root Mean Squares (RMS) errors in terms of the project's survey coordinates for checkpoints as determined by the ground scale of the map. The standard also provides three sets of accuracy figures for maps produced with different accuracy levels (Abdullah, 2013).

Limiting RMSE (m)	
Scale	ASPRS
1:1000	0,254
1:2500	0,635
1:5000	1,27

Table 1: Examples of the limiting planimetric RMS for the three accuracy standards

Summing up the above, is concluded that the NSSDA and JRC accuracy standards are not true standards in the same sense the ASPRS standards were meant to be. The NSSDA and JRC standards are closer to guidelines as they define testing methodology and statistical analysis guidelines. These guidelines, do not determine pass/fail criteria which are left to the users. However, based on NSSDA standard and ASPRS limiting RMSEs, the Horizontal accuracy for an orthophoto with a scale of 1:5000 is specified as :

$$NSSDA_h = 1.73 \times RMSE_r = 1.73 \times 1.27 = 2.20m.$$

3.2.4. Checkpoints Selection and Distribution

According to the NSSDA and JRC Guidelines, accuracy testing should be performed using an independent source of higher positional accuracy.

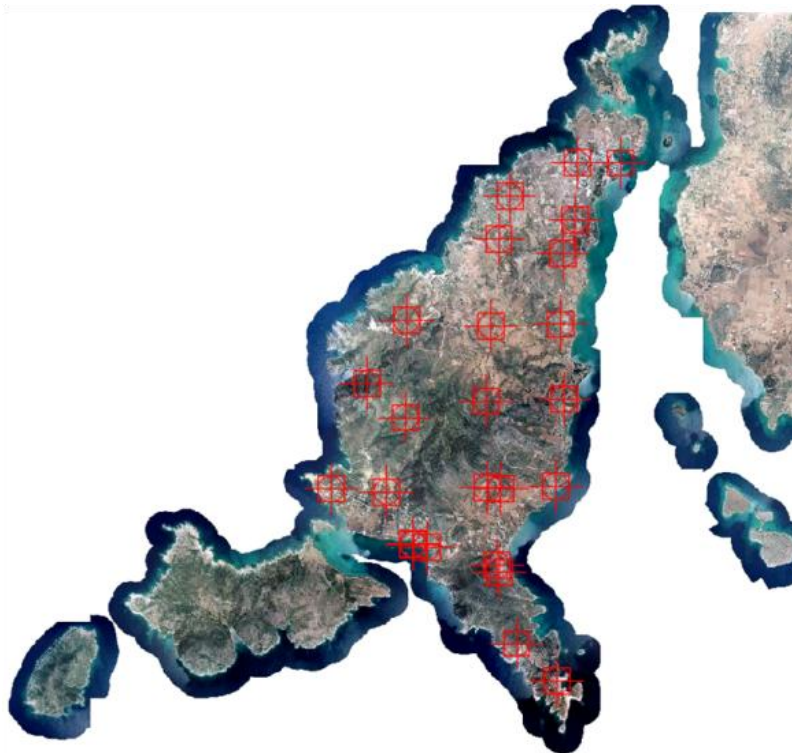


Figure 14: Checkpoints distribution on GeoEye-1 orthophoto

The accuracy of the independent test points should fall within one-third of the intended accuracy (95% confidence level) of the examined dataset. A minimum of 20 well defined test points should be used to evaluate the accuracy of the dataset. The check points will be ideally evenly distributed and located across the image. The selected check point positions may be located with reference to the positions of the GCPs used to correct the imagery in order to ensure that the two sets of points are independent (CPs should not be close to the GCPs).

The location or the distribution of the checkpoints is also specified in NSSDA and JRC guidelines. These Standards assume that the area to be evaluated is a rectangle and is divided into four quads and a diagonal is to be established across the area. At least 20% of the points should lie in each quarter whereas the optimum distance between points (is related to the diagonal distance of the area (1/10th of the diagonal length which for this case is $1/10 \times 15\text{km} = 1.5\text{km}$).

3.3. Measurements - Results

25 checkpoints were measured and used for the Pleiades 1B dataset and 26 checkpoints were used for the GeoEye-1 and LSO data scattered into areas with different terrain relief and land cover. It is noted that for Pleiades 1B was determined 1 checkpoint less due to the clouds over the area of the point. The coordinates of these checkpoints were determined on the control dataset, the aerial imagery orthophoto (VLSO) provided from Hellenic National Cadastre & Mapping Agency S.A. (NCMA S.A) (0.25m GSD) from August 2012.

A/A	VLSO (Control Dataset)		LSO		GEOEYE 1		PLEIADES B1	
	X(m)	Y(m)	dX(m)	dY(m)	dX(m)	dY(m)	dX(m)	dY(m)
1	596781,77	4100183,44	0,236	0,47	-0,558	1,121	-0,69	-0,28
2	595845,18	4100188,57	-0,39	0,348	-0,016	0,885	-0,73	-0,02
3	595813,14	4098975,4	0,291	0,396	-0,176	1,239	-0,05	-0,17
4	594419,04	4099474,79	0,515	1,089	-0,235	0,46	0,51	-0,09
5	595546,93	4098254,51	0,839	0,858	-0,235	0,788	-0,37	0,23
6	594187,66	4098555,68	-0,19	-0,097	-0,337	0,079	-0,23	-0,78
7	595494,5	4096742,6	-0,29	0,871	-0,581	1,067	-0,45	0,49
8	595406,89	4096729,21	0,305	0,405	0,583	1,516	-0,28	-0,04
9	594027,42	4096706,9	0,106	0,262	0,279	0,27	-0,63	-0,7
10	592307,54	4096692,48	-0,022	0,886	-0,141	0,995	-0,09	-0,72
11	592229,01	4096831,51	0,159	0,81	0,001	1,071	-0,5	-0,68
12	595570,94	4095148,65	-0,565	1,119	-0,113	-0,912	-0,65	0,15
13	593924,05	4095109,99	-0,359	0,912	-0,661	0,327	0,39	-0,51
14	592201,41	4094754,63	-0,191	0,567	-0,444	0,726	-0,38	0,04
15	591581,53	4095387,22	-0,388	0,639	-0,348	0,783	-0,51	-0,6
16	591386,71	4095474,95	0,021	0,736	0,856	1,037	0,47	-0,14
17	595389,69	4093290,39	-0,361	0,071	0,079	-1,311	-	-
18	593939,63	4093262,95	-0,552	0,161	0,727	0,009	0,69	-0,56
19	591828,22	4093270,46	-0,677	-0,196	-1,482	-0,457	-0,77	-0,55
20	591811,63	4093172,45	-0,404	0,201	-0,571	0,406	-0,51	-0,2
21	590625,15	4093229,84	-0,445	0,701	-0,366	0,947	0,18	-0,91
22	592663,35	4091993,05	-0,136	0,544	-0,221	0,705	0,11	0,26
23	592370,47	4092052,04	-0,123	0,364	-0,132	0,981	0,09	0,49

24	592357,15	4092062,4	-0,707	0,47	-0,084	0,676	0,22	0,04
25	594197,98	4091451,92	-0,056	-0,337	-0,271	0,182	-0,28	-0,28
26	595326,84	4089050,41	-0,045	0,043	-0,44	0,29	-0,16	0,61

Table 2: Measured coordinates for GeoEye-1 and Pleiades 1B orthoimagery. ¹

The results are presented with a statistical analysis and they are evaluated in order to present the merits and demerits of the imaging sensors involved. To this direction the Standard Deviation (σ) or sigma are computed as an indicator of how well the measurements fit each other and a measure of precision. In addition, the Root Mean Squares Error (RMSE) is computed for Northing and Easting coordinates. It is assumed that errors in the spatial data have random behavior and that systematic errors have been eliminated as best as possible.

RESIDUALS			
ΔX			
	Pleiades B1	Geoeye-1	LSO
Check Pts	25	26	26
StDEV(m)	0.374	0.388	0.467
RMSE_X(m)	0.389	0.607	0.495
ΔY			
	Pleiades B1	Geoeye-1	LSO
Check Pts	25	26	26
StDEV (m)	0.658	0.415	0.423
RMSE_Y(m)	0.838	0.453	0.465

Table 3. Resulting residuals of the measured checkpoints

As observed, in aerial imagery LSO and Geoeye-1 orthoimage, the Standard Deviation and RMSE_{X,Y} differ indicating a systematic error in Y axis. Thus, a bias removal procedure was applied in order to evaluate orthoimages objectively and accurately.

The BIAS is estimated by the formula:

$$BIAS = \sqrt{RMSE_{XY}^2 - \sigma^2} \quad (5)$$

where σ = is the random error

Data Source	Pleiades B1		Geoeye-1		LSO	
RMS_{x,y} - stdev	0,038	0,042	0,028	0,179	0,016	0,219
Linear Bias	0,181	0,193	0,164	0,518	0,110	0,467
Circular Bias	0,265		0,543		0,479	

Table 4: Bias calculations

	Pleiades B1	Geoeye-1	LSO
RMSE_X(m)	0.522	0.381	0.578

¹ The differences dX,Y, are computed as $dX, Y = X, Y_{data} - X, Y_{check}$

RMSE_Y(m)	0.6455	0.453	0.465
HR RESIDUALS			
	Pleiades B1	Geoeye-1	LSO
RMSE_{XY}(m)	0.646	0.866	0.649

Table 5: RMSEs and residuals after bias removal

Geoeye-1 data have the larger RMSE_{XY} possibly due to bad image quality leading to erroneous GCPs measurements on the images. Pleiades 1B orthoimage has almost the same external accuracy as the orthoimage from aerial imagery (LSO from NCMA S.A.).

All the tested orthoimages are adequate for producing LSO according to the NSSDA Standards, the GRC Guidelines and the ASPRS Standards. In addition, Pleiades 1B orthoimagery seems to be adequate for a scale of 1:2500 according to ASPRS Standards.

3.4. Conclusion

The main aim of this Part I was to assess the geometric and radiometric quality of orthorectified high resolution satellite imagery from Pleiades-1B satellites through a comparative evaluation of their quantitative and qualitative properties. In addition, the advantages and limits of the Pleiades Imaging for producing Large Scale Orthophotos (LSO) are investigated. Through the visual assessment of the orthoimagery revealed that Pleiades 1B orthoimagery is especially prominent presenting much more information and clearer forms. On the contrary, abrupt changes of brightness and contrast and high radiometric saturation levels were observed on the GeoEye-1 orthomosaic. Both radiometric and accuracy test results show that Pleiades 1B orthoimage has almost the same absolute accuracy as the orthoimage from aerial imagery (LSO from Hellenic National Cadastre & Mapping Agency S.A.). Hence, it could easily replace aerial imagery, when it comes to orthophoto production. Furthermore, all data are adequate for producing LSO for mapping and GIS, according to JRC and NSSDA accuracy standards. The results also serve for a critical approach for the usability and cost efficiency of satellite imagery for the production of LSO.

Part II

The effect of Pansharpening Algorithms on Digital
Surface Model Extraction and Resulting
Orthoimagery

CHAPTER 4

Introduction

Satellite optical sensors provide very valuable data about the Earth surface through map-making and environmental monitoring. However, these applications are extremely expensive and the scientific community should use this data obtained from available sensors in the best way.

A typical example of this is the pansharpening process, i.e. the fusion of multispectral satellite imagery of low spatial and high spectral resolution with the panchromatic imagery of high spatial and low spectral resolution. In recent years, pansharpening has become a task of great importance in the field of data fusion, as demonstrated by the increasing number of scientific contributions to this topic. Pansharpening addresses the fusion of two optical remote sensing images characterized by different spectral and spatial features. Specifically, a Multi Spectral (MS) image with high spectral but low spatial resolution is considered along with a Panchromatic (PAN) image, which is obtained by sensing a single wide electromagnetic spectrum covering the visible and near infrared (VNIR) frequencies and has complementary characteristics with respect to MS: lower spectral but greater spatial resolution.

Due to cost and complexity issues and limited onboard storage capabilities, the multispectral sensor has much smaller aperture than the panchromatic sensor thus reducing the spatial resolution of the sensed multispectral image (Shaw and Burke, 2003). In addition, the multispectral sensor has a larger pixel size in order to capture the MS content. For a typical modern multispectral satellite sensor, this ratio is 1 to 16, i.e., a single multispectral image pixel translates to 4 by 4 panchromatic pixels.

Pansharpening is the fusion of the images captured by the multispectral and panchromatic sensors. The objective of pansharpening algorithms is the generation of a fused product characterized by the spectral content of the MS image and the spatial details of the PAN image. This means that the pansharpened image has the same number of pixels as the panchromatic image and also the same number of bands as the multispectral image.

This chapter investigates the geometric effects of pansharpening algorithms on automatically generated DSMs and thus the resulting orthoimagery. The motivation for this investigation is that on automatically generated Digital Surface Models, image correlation is used to extract matching pixels in overlapping images. Thus their accuracy is strictly related to image quality. The Pansharpening process sometimes results in bad image quality and may affect the DSM generation and then the resulting orthoimage accuracy. To this direction, an iterative methodology was applied in order

to combine the methodology described in Part I with different pansharpening algorithms and check the accuracy of orthoimagery resulting from pansharpened data.

CHAPTER 5

Methodology

Having already exploited and measured a benchmark dataset, the orthomosaic of N.C.M.A. S.A. of 0.25m GSD (VLSO), was decided to use the same Control Points described in 0 and compare the measurements with measurements on the new Orthoimagery, produced from pansharpened images.

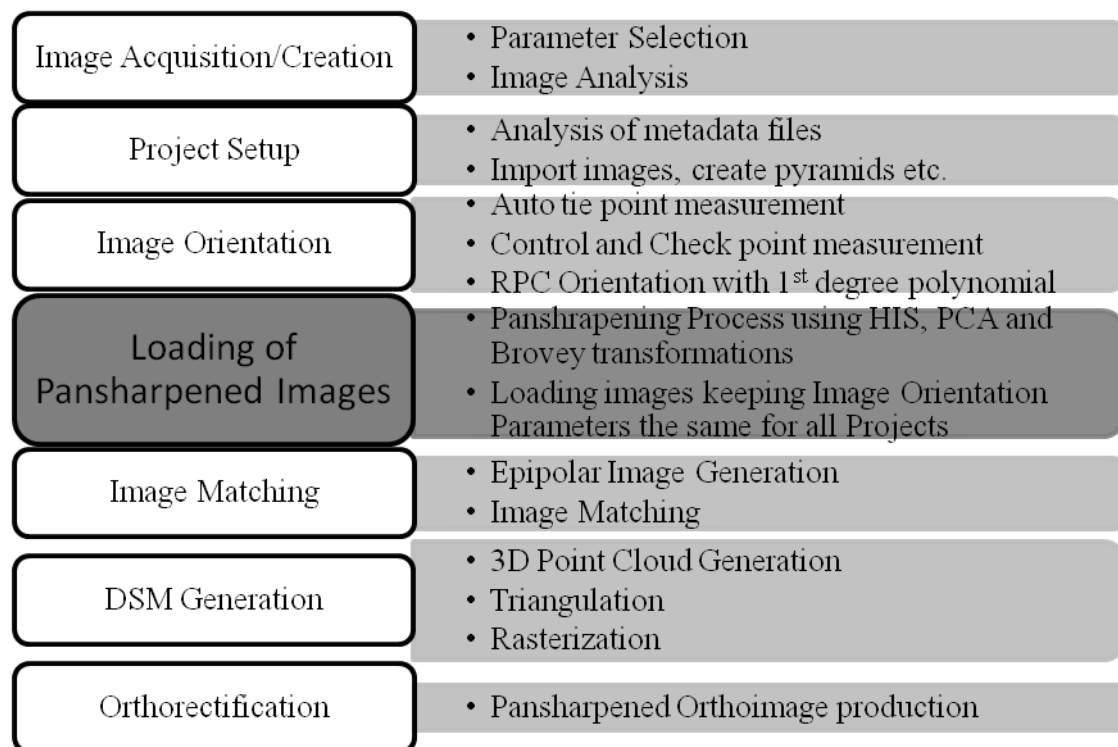


Figure 15: Workflow chart for checking the effects of pansharpening process

To this end, the classical photogrammetric workflow available in ERDAS Photogrammetry Tool (former LPS) environment (ERDAS 2014) was followed for the processing of the stereo satellite imagery, DSM generation and orthorectification.

In addition to the workflow applied in Part I, pansharpening procedures were performed between the stages of Image Orientation and Image Matching. At that stage, the pansharpened imagery created using HIS, PCA and Brovey transformations was replacing the PAN imagery, changing the file location. In this way, the initial Image Orientation Parameters remained the same for the whole block in order to produce more objective and reliable results. Thus, the only parameter differentiated, is the source image which may lead to different image matching for DSM generation.

5.1. Pansharpening Algorithms

In recent years, pansharpening has become a task of great importance in the field of data fusion, as demonstrated by the increasing number of scientific contributions to this topic. It is possible to group the various pansharpening methods into two main families (Aiazzi et al., 2012):

- i. The methods based on the projection of the MS image into a new space and the substitution of a component with a histogram matched version of the PAN image (the so-called Component Substitution (CS) class) and
- ii. The approaches based on the extraction of spatial details from the PAN image and their injection into the MS one (this class is called Multi-Resolution Analysis (MRA) because details are usually obtained through a multiscale decomposition of the original image).

There are also hybrid methods based on both MRA and CS. Then there are methods based on variation techniques, such as the P+XS method.

Widely known examples of the CS methods are Intensity Hue Saturation (Haydn et al., 1982), Principal Component Analysis (Chavez and Kwarteng, 1989, Shah et al., 2008) and Gram-Schmidt (GS) (Laben and Brower, 2000) techniques. MRA methods are usually based on methods such as the Undecimated Discrete Wavelet Transform (UDWT) or other kinds of pyramidal or multi-scale representations. A more systematic overview of pansharpening methodologies belonging to these two categories can be found in (Thomas et al., 2008) and (Aiazzi et al., 2012).

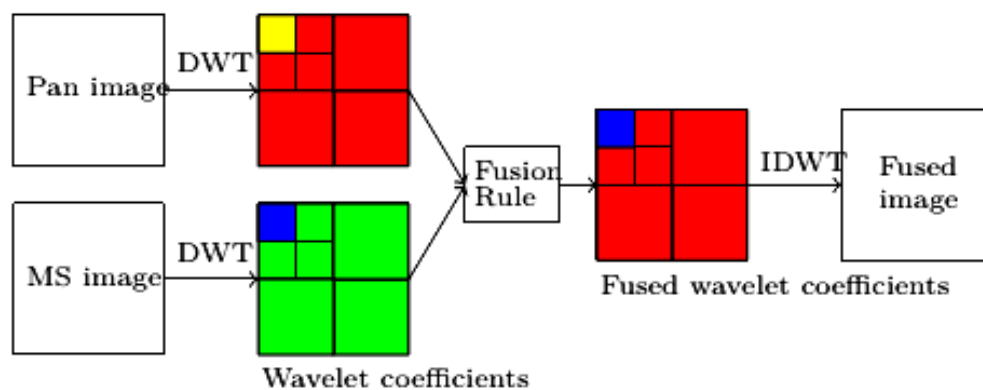


Figure 16: Basic wavelet based pansharpening (Palsson et al., 2012)

Moreover, in the last years, approaches that do not fit in this classification have started to appear in the literature. Among those, we can list Bayesian methods based on parameter estimation total variation penalization terms and sparse signal representation (Fasbender et al., 2008; Palsson et al., 2014; Li and Yang, 2011; Zu and Bamler, 2013).

5.1.1. Implemented Algorithms and Results

Initially, it was decided to check state of the art pansharpening algorithms such as HCS, IHS and HPF. However, this decision was never realized since pansharpening

procedures in ERDAS Imagine 2014 using the already described Pleiades 1B data produce images of wrong dimensions². To overcome this problem, pansharpening was performed using the Photomod photogrammetric software by Racurs. This software offers the three commonly used methods, although they are not considered the state of the art: the Brovey transform, the IHS (Intensity, Hue, Saturation) method, and the PCA (Principal Component Analysis) method. The Brovey transform is based on spectral modeling, while the IHS and PCA methods call upon projection techniques.. These methods are available in most commercial software packages for satellite image processing, which may explain their extensive use by practitioners. Here the ERDAS Imagine software was used for their application. Details on these methods can be found in e.g., Carper et al. (1990) or Pohl and Van Genderen (1998).

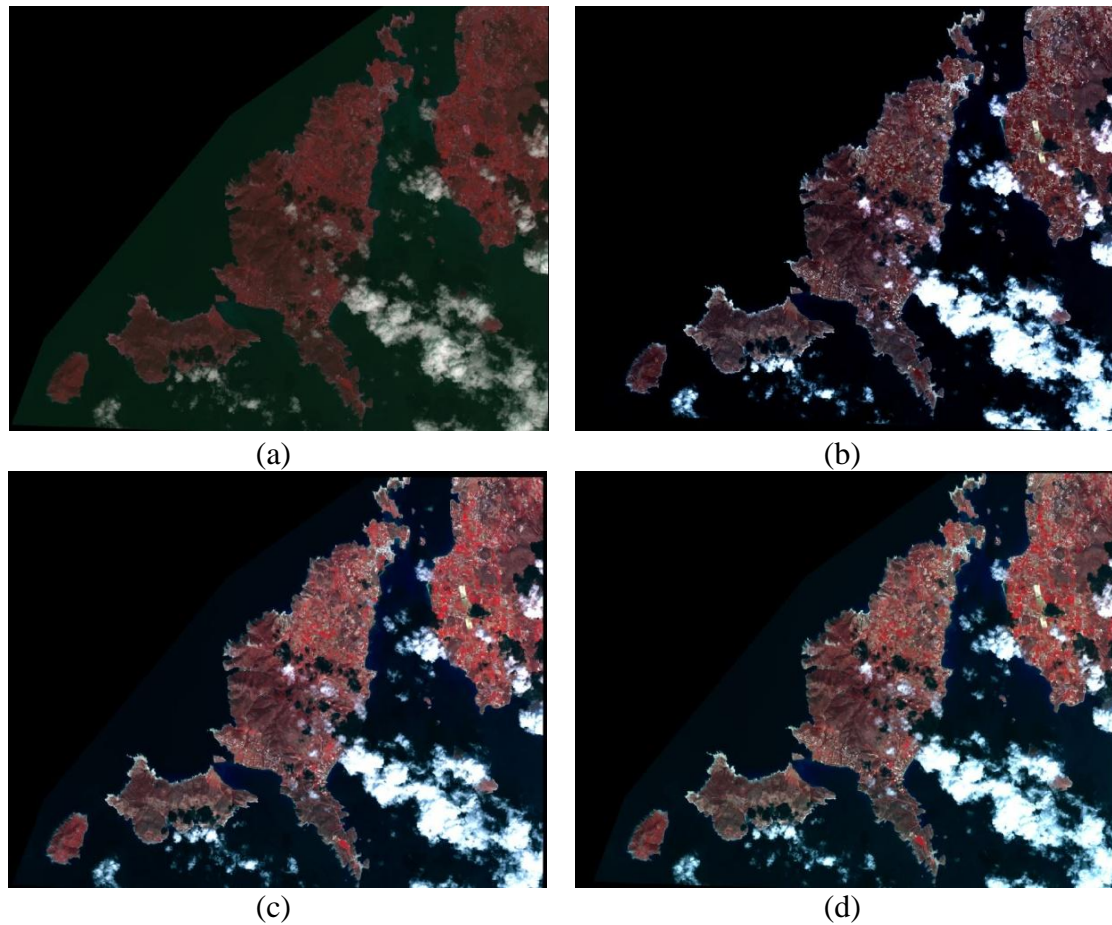


Figure 17: The original MS image (a) and the Pansharpening results from IHS (b), Brovey (c) and PCA (d) algorithms.

5.1.1.1 PCA (Principal Component Analysis)

Principal Components Substitution, is a widely known method belonging in the aforementioned CS family that relies on the Principal Component Analysis (PCA) mathematical transformation. The PCA is also known as the Karhunen-Loève transform or the Hotelling transform and is widely used in signal processing, statistics and many other areas. The transformation generates a new set of rotated axes, in

² In order to overcome this problem, which probably lies in the metadata files of Pleiades 1B, the Airbus Defence and Space Customer Technical Support (CustomerTechnicalSupport@spotimage.fr) was informed and we asked for a solution.

which the new image spectral components are not correlated. The largest amount of the variance is mapped to the first component, with decreasing variance going to each of the following ones. The sum of the variances in all the components is equal to the total variance present in the original input images (Amro et al., 2011). PCA and the calculation of the transformation matrices can be performed following the steps specified by Gonzalez and Woods in (Gonzalez and Woods, 2008).

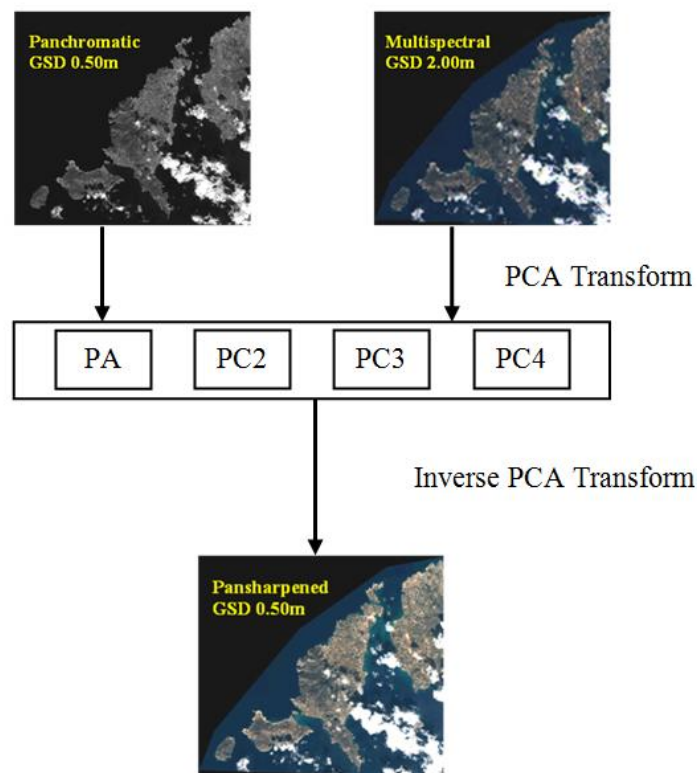


Figure 18: PCA based Pansharpening

Based on theory, the first principal component, PC1, collects the information that is common to all bands used as input data to the PCA, i.e., the spatial information, while the spectral information that is specific to each band is captured in the other principal components (Chavez and Kwarteng, 1989). This makes PCS an adequate technique when merging MS and PAN images. PCS is similar to the IHS method, with the main advantage that an arbitrary number of bands can be considered. However, some spatial information may not be mapped to the first component, depending on the degree of correlation and spectral contrast existing among the MS bands, resulting in the same problems that IHS had (Chavez and Kwarteng, 1989).

5.1.1.2 Brovey Transform

The Brovey transformation or Brovey fusion, named after its author, allows the merging of data from different sensors by a simple way and uses ratios to sharpen the multispectral (MS) image (Pohl and Van Genderen, 1998). In this method, the MS image is normalized and each band of the fused MS image is obtained by multiplying the normalized MS bands with the panchromatic image. The Brovey transform provides excellent contrast in the image domain but greatly distorts the spectral characteristics (Vijayaraj et al., 2004).

Each channel of the fused image is computed as:

$$F(n) = N PAN \frac{MS(n)}{\sum_{k=1}^N MS(k)}$$

where $F(n)$ and $MS(n)$ are the n -th channels of the fused and MS images respectively and N is the number of channels in the MS image.

5.1.1.3 IHS (Intensity Hue Saturation)

The Intensity-Hue-Saturation (IHS) method (Haydn et al., 1982) has been widely used (Carper et al., 1990, Chavez and J. Bowell, 1988, Edwards and P. Davis 1994, Tu et al., 2004) for pansharpening satellite images. In this frequently used method, a component derived from the MS image is substituted for a component derived from the PAN image and then the fused or pansharpened image is obtained from the inverse transformation. The basic idea is to first transform the MS image into intensity (I), hue (H) and saturation (S) components (IHS colour space).

$$\begin{bmatrix} I \\ H \\ S \end{bmatrix} = \begin{bmatrix} \frac{1}{3} & \frac{1}{3} & \frac{1}{3} \\ -\frac{\sqrt{2}}{6} & -\frac{\sqrt{2}}{6} & \frac{\sqrt{2}}{6} \\ \frac{1}{2} & \frac{1}{2} & 0 \end{bmatrix} \begin{bmatrix} R \\ G \\ B \end{bmatrix}$$

The next step is to adjust the Pan image so that it has the same mean and variance as the intensity component of the MS image.

$$P = \frac{\sigma_I}{\sigma_P} (P - m(P) + \mu(I))$$

The intensity component is then replaced with the appropriately scaled Pan image and finally the inverse IHS transformation is taken to get the fused image. The IHS method produces images that have high spatial resolution and low spectral quality (Palsson et al., 2012).

$$\begin{bmatrix} F(R) \\ F(G) \\ F(B) \end{bmatrix} = \begin{bmatrix} R + P - I \\ G + P - I \\ B + P - I \end{bmatrix}$$

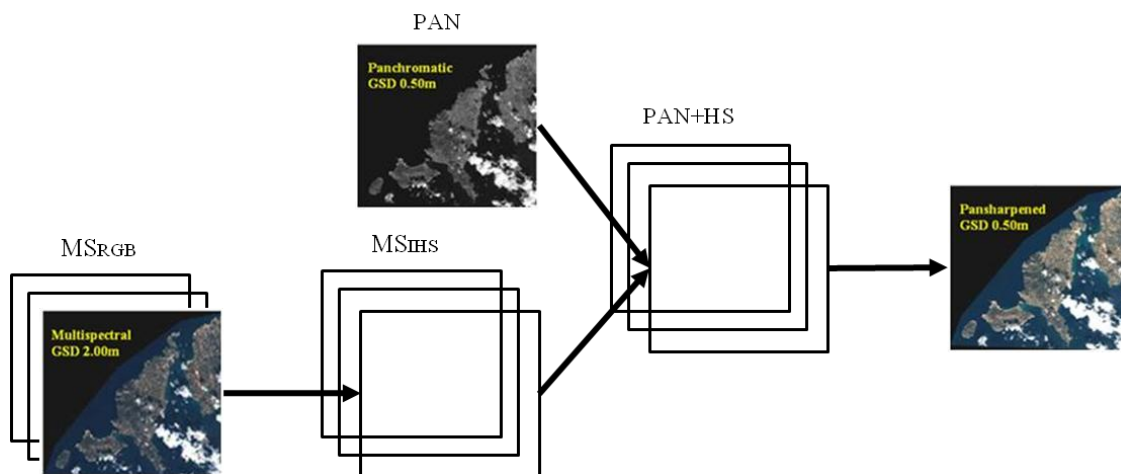


Figure 19: Standard IHS fusion scheme



(a)



(b)



(c)



(d)

Figure 20: A zoom of the original MS image (a) and the Pansharpening results from IHS (b), Brovey (c) and PCA (d) algorithms for 4 Bands.

5.2. Automatic DSM Generation

Even if the same procedure is applied on processing stage of Part I, the automatic DSM generation stage or Automatic Terrain Extraction (ATE) is described here in order to understand better how the Pansharpening process may affect the extracted DSM and thus the resulting Orthoimagery.

In the literature several techniques are presented suitable for DSM extraction. Some of them are based on digital aerial and terrestrial photogrammetry, airborne and terrestrial laser scanning, GPS methodology with its different measurement approaches and active and passive remote sensing, with optical satellite imagery systems (Fraser et al., 2002). In particular, aerial and satellite photogrammetry is a powerful tool in surface model generation extracting high resolution DSMs by means of automated image matching procedures. For these tools, DSM can be either vector or raster format and its density ranges from 1/3 to 1/10 of density of original image pixels.

The standard procedures to generate DSMs are based on fundamental steps which consist in internal orientation, external orientation (registration into a defined reference system) and point extraction. For the tests performed in the context of this Thesis, the standard procedures described above are the same for all blocks. The only parameter which is differentiated is the used imagery and thus the extracted points.

The seven different DSMs of which six of them are presented in Figure 22, were generated in the ERDAS LPS module Classic ATE (Classic Automatic Terrain Extraction) with stereo image matching, which aims at finding dense and robust correspondences between stereo images and estimate their 3D coordinates in object space. Since the elevation interval was chosen to be 10 meters and the external accuracy of the buildings was not to be checked, there was no need of using the eATE tool of the software which is more time consuming. The matching procedure in Classic ATE is pyramid based, that is, it starts from high-pyramid levels and

continues to low pyramid levels. At each level the search range used stays the same on image space but is actually reduced to half on object space, which means search range goes smaller and smaller by brute-force. This method is proven to be a reliable solution (Xu et al., 2008) since the approach is based on multi-band image matching for increasing the precision of the results.

Since this automatic DSM generation approach of the used software is mainly characterised by the feature-based matching technique being hierarchically applied in image pyramids and a robust surface reconstruction with finite elements, it is expected the resulting DSMs from different pansharpened data to be differentiated between them.

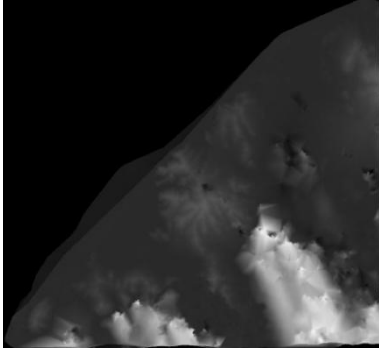
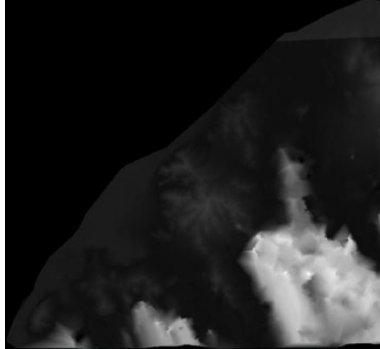
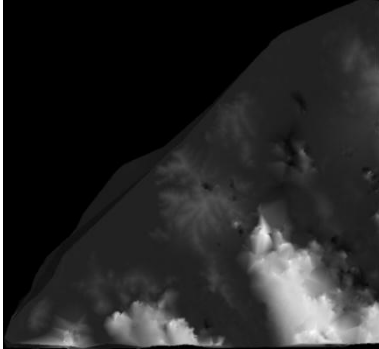
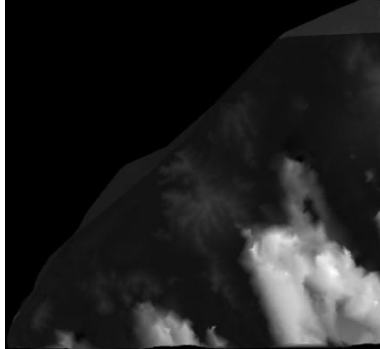
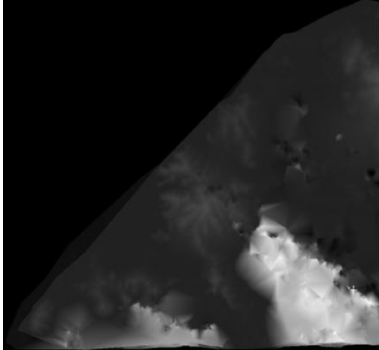
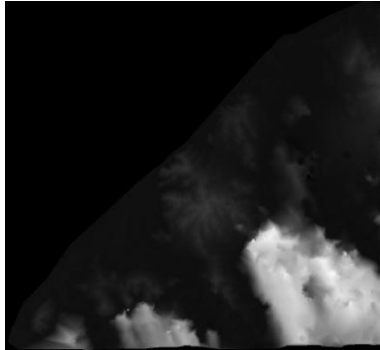
Pansharpening Algorithm	3 Bands (RGB)	4 Bands (RGB-NIR)
IHS		
PCA		
BROVEY		

Figure 21: DSMs from different pansharpened data

Remarkable is that all the DSMs resulting from the 4-Band Pansharpened data are displayed by almost the same grey values. However, these values are differentiated by

the values consisting the DSMs resulting from the 3-Band data. This probably occurs due to the existence of the 4th Band, the NIR band.

CHAPTER 6

Accuracy Assessment of Pansharpening Algorithms

In order to assess and compare the pansharpening algorithms in terms of accuracy, the same 25 checkpoints as in Part I were measured on the resulting orthoimagery. In more detail, the 25 checkpoints were measured on the orthoimagery created using the IHS, PCA and BROVEY pansharpening algorithms for three bands (RGB) and four bands (RGB-NIR). The coordinates of these checkpoints were determined on the control dataset, the aerial imagery orthophoto (VLSO) provided from Hellenic National Cadastre & Mapping Agency S.A. (NCMA S.A) (0.25m GSD) from August 2012 and also on the orthoimagery created using the Panchromatic data. The results are presented with a statistical analysis and they are evaluated in order to present the merits and demerits of the imaging sensors involved. To this direction the Standard Deviation (σ) or sigma are computed as an indicator of how well the measurements fit each other and a measure of precision. In addition, the Root Mean Squares Error (RMSE) is computed for Northing and Easting coordinates. It is assumed that errors in the spatial data have random behavior and that systematic errors have been eliminated as best as possible.

6.1. VLSO and Pleiades 1B PMS-N (IHS-PCA-BROVEY) Accuracy Comparison

6.1.1. Four Band Data (RGB and NIR)

A/A	VLSO (Control Dataset)		IHS 4		PCA 4		BROVEY 4	
	X(m)	Y(m)	dX(m)	dY(m)	dX(m)	dY(m)	dX(m)	dY(m)
1	596781,77	4100183,44	-0,72	-0,73	-0,86	-0,66	-0,79	-0,44
2	595845,18	4100188,57	-0,84	-0,25	-0,53	-0,2	-1,02	-0,22
3	595813,14	4098975,4	-0,64	-0,40	-0,68	-0,18	-0,49	-0,2
4	594419,04	4099474,79	0,74	-0,29	0,40	-0,18	-0,18	-0,09
5	595546,93	4098254,51	-0,09	0,36	-0,21	0,46	-0,19	0,35
6	594187,66	4098555,68	-0,65	-1,05	-0,70	-0,79	-0,47	-1,15
7	595494,5	4096742,6	-0,08	0,94	0,07	0,64	0,13	2,05
8	595406,89	4096729,21	-0,40	-0,11	-0,32	-0,12	-0,43	-0,14
9	594027,42	4096706,9	-0,11	-0,41	-0,78	-0,24	-0,52	-0,41
10	592307,54	4096692,48	-0,29	-0,47	-0,25	-0,88	0,08	-0,3
11	592229,01	4096831,51	-0,48	-0,79	-0,34	-0,89	-0,23	-0,6

12	595570,94	4095148,65	-0,30	0,30	-0,24	0,44	-0,56	0,24
13	593924,05	4095109,99	-0,56	0,86	-0,01	-0,11	0,31	-0,61
14	592201,41	4094754,63	-0,54	-0,95	-0,99	-0,45	-0,66	-1,26
15	591581,53	4095387,22	-0,23	0,28	-0,46	0,13	-0,56	0,24
16	591386,71	4095474,95	-0,65	-0,50	-0,42	-0,57	-0,55	-0,69
17	595389,69	4093290,39	0,70	0,13	0,77	-0,11	0,85	0,12
18	593939,63	4093262,95	0,21	-0,01	-0,80	-0,98	0,52	-0,19
19	591828,22	4093270,46	-1,03	-0,69	-1,15	-1,06	-0,86	-0,67
20	591811,63	4093172,45	-0,49	0,01	-0,42	0,02	-0,15	0,26
21	590625,15	4093229,84	-0,52	-0,25	-0,82	-0,3	-0,45	-0,43
22	592663,35	4091993,05	0,28	0,60	0,31	0,54	0,57	0,77
23	592370,47	4092052,04	0,01	0,13	-0,07	0,60	-0,02	0,39
24	592357,15	4092062,4	0,22	0,38	0,13	0,32	0,46	0,63
25	594197,98	4091451,92	-0,17	0,14	-0,13	-0,4	-0,09	-0,23

Table 6: Measured coordinates for Pleiades 1B orthoimagery created from 4 bands data and compared with the VLSO.³

RESIDUALS			
ΔX			
	IHS 4	PCA 4	BROVEY 4
Chck Pts	25	25	25
StDEV(m)	0,437	0,454	0,472
RMSE _X (m)	0,511	0,567	0,517
ΔY			
	IHS 4	PCA 4	BROVEY 4
Check Pts	25	25	25
StDEV (m)	0,523	0,501	0,657
RMSE _Y (m)	0,534	0,539	0,666

Table 7: Resulting residuals of the measured checkpoints

6.1.2. Three Band Data (RGB)

VLSO (Control Dataset)		IHS 3		PCA 3		BROVEY 3		
A/A	X(m)	Y(m)	dX(m)	dY(m)	dX(m)	dY(m)	dX(m)	dY(m)
1	596781,77	4100183,44	-0,74	-0,26	-0,91	0,08	-0,91	-0,44
2	595845,18	4100188,57	-1,02	-0,27	-1,23	-0,22	-1,12	-0,11
3	595813,14	4098975,4	-0,60	-0,10	-0,70	-0,20	-0,54	-0,26
4	594419,04	4099474,79	0,24	-0,50	0,45	-0,30	0,24	-0,19
5	595546,93	4098254,51	-0,31	0,35	-0,31	0,58	-0,19	0,58
6	594187,66	4098555,68	-0,41	-1,03	-0,59	-1,21	-0,53	-1,27
7	595494,5	4096742,6	-0,68	0,98	-0,61	0,77	-0,68	1,45
8	595406,89	4096729,21	-0,21	0,14	-0,28	0,05	-0,40	-0,08
9	594027,42	4096706,9	-0,46	-0,19	-0,85	-0,36	-0,57	-0,58
10	592307,54	4096692,48	-0,20	-0,74	-0,15	-0,64	-0,15	-0,56
11	592229,01	4096831,51	-0,27	-0,79	-0,30	-0,85	-0,33	-0,82

³ The differences dX, Y , are computed as $dX, Y = X, Y_{data} - X, Y_{check}$

12	595570,94	4095148,65	-0,70	0,10	-0,56	0,10	-0,49	0,30
13	593924,05	4095109,99	-0,09	-0,91	0,01	-0,50	-0,09	-1,11
14	592201,41	4094754,63	-0,42	-1,26	-0,10	-1,34	-0,18	-1,18
15	591581,53	4095387,22	-0,19	0,30	-0,31	0,30	-0,01	0,66
16	591386,71	4095474,95	-0,50	-0,54	-0,55	-0,69	-0,45	-0,39
17	595389,69	4093290,39	0,73	0,12	0,85	0,18	0,79	0,24
18	593939,63	4093262,95	0,43	-0,29	0,52	-0,29	0,81	-0,19
19	591828,22	4093270,46	-1,23	-0,83	-1,17	-0,77	-1,07	-0,77
20	591811,63	4093172,45	0,09	0,18	-0,31	0,22	-0,43	0,10
21	590625,15	4093229,84	-0,67	-0,38	-0,56	-0,32	-0,34	-0,21
22	592663,35	4091993,05	0,57	0,71	0,33	0,77	0,51	0,29
23	592370,47	4092052,04	-0,13	0,50	0,09	0,35	0,09	0,39
24	592357,15	4092062,4	0,13	0,30	0,13	0,30	0,24	0,63
25	594197,98	4091451,92	-0,12	-0,12	-0,16	-0,05	-0,16	-0,16

Table 8: Measured coordinates for Pleiades 1B orthoimagery created from 3 bands data and compared with the VLSO.

RESIDUALS			
ΔX			
	IHS 3	PCA 3	BROVEY 3
Chck Pts	25	25	25
StDEV(m)	0,460	0,502	0,489
RMSE _X (m)	0,534	0,580	0,544
ΔY			
	IHS 3	PCA 3	BROVEY 3
Check Pts	25	25	25
StDEV (m)	0,551	0,547	0,628
RMSE _Y (m)	0,580	0,570	0,645

Table 9: Resulting residuals of the measured checkpoints

6.2. Pleiades 1B PAN and Pleiades 1B PMS-N (IHS-PCA-BROVEY) Accuracy Comparison

6.2.1. Four Band Data (RGB and NIR)

PANCHROMATIC			IHS 4		PCA 4		BROVEY 4	
A/A	X(m)	Y(m)	dX(m)	dY(m)	dX(m)	dY(m)	dX(m)	dY(m)
1	596781,08	4100183,16	-0,03	-0,45	-0,17	-0,38	-0,10	-0,16
2	595844,45	4100188,55	-0,11	-0,23	0,2	-0,18	-0,29	-0,20
3	595813,09	4098975,23	-0,59	-0,23	-0,63	-0,01	-0,44	-0,03
4	594419,55	4099474,70	0,23	-0,20	-0,11	-0,09	-0,69	0,00
5	595546,56	4098254,74	0,28	0,13	0,16	0,23	0,18	0,12
6	594187,43	4098554,90	-0,42	-0,27	-0,47	-0,01	-0,24	-0,37
7	595494,05	4096743,09	0,37	0,45	0,52	0,15	0,58	1,56
8	595406,61	4096729,17	-0,12	-0,07	-0,04	-0,08	-0,15	-0,10
9	594026,79	4096706,20	0,52	0,29	-0,15	0,46	0,11	0,29

10	592307,45	4096691,76	-0,20	0,25	-0,16	-0,16	0,17	0,42
11	592228,51	4096830,83	0,02	-0,11	0,16	-0,21	0,27	0,08
12	595570,29	4095148,80	0,35	0,15	0,41	0,29	0,09	0,09
13	593924,44	4095109,48	-0,95	1,37	-0,4	0,40	-0,08	-0,10
14	593880,55	4095209,32	-0,53	0,77	-0,98	1,27	-0,65	0,46
15	592201,03	4094754,67	0,15	0,24	-0,08	0,09	-0,18	0,20
16	591581,02	4095386,62	-0,14	0,1	0,09	0,03	-0,04	-0,09
17	591387,18	4095474,81	0,23	0,27	0,3	0,03	0,38	0,26
18	593940,32	4093262,39	-0,48	0,55	-1,49	-0,42	-0,17	0,37
19	591827,45	4093269,91	-0,26	-0,14	-0,38	-0,51	-0,09	-0,12
20	591811,12	4093172,25	0,02	0,21	0,09	0,22	0,36	0,46
21	590625,33	4093228,93	-0,70	0,66	-1,00	0,61	-0,63	0,48
22	592663,46	4091993,31	0,17	0,34	0,2	0,28	0,46	0,51
23	592370,56	4092052,53	-0,08	-0,36	-0,16	0,11	-0,11	-0,10
24	592357,37	4092062,44	0,00	0,34	-0,09	0,28	0,24	0,59
25	594197,70	4091451,64	0,11	0,42	0,15	-0,12	0,19	0,05

Table 10: Measured coordinates for Pleiades 1B orthoimagery created from 4 bands data and compared with the one created using the Panchromatic data.

RESIDUALS			
ΔX			
	IHS 4	PCA 4	BROVEY 4
Check Pts	25	25	25
StDEV(m)	0,357	0,460	0,311
RMSE _X (m)	0,367	0,487	0,310
ΔY			
	IHS 4	PCA 4	BROVEY 4
Check Pts	25	25	25
StDEV (m)	0,399	0,360	0,376
RMSE _Y (m)	0,437	0,372	0,414

Table 11: Resulting residuals of the measured checkpoints

6.2.2. Three Band Data (RGB)

PANCHROMATIC		IHS 3		PCA 3		BROVEY 3		
A/A	X(m)	Y(m)	dX(m)	dY(m)	dX(m)	dY(m)	dX(m)	dY(m)
1	596781,77	4100183,44	-0,05	0,02	-0,22	0,36	-0,22	-0,16
2	595845,18	4100188,57	-0,29	-0,25	-0,50	-0,20	-0,39	-0,09
3	595813,14	4098975,4	-0,55	0,07	-0,65	-0,03	-0,49	-0,09
4	594419,04	4099474,79	-0,27	-0,41	-0,06	-0,21	-0,27	-0,10
5	595546,93	4098254,51	0,06	0,12	0,06	0,35	0,18	0,35
6	594187,66	4098555,68	-0,18	-0,25	-0,36	-0,43	-0,30	-0,49
7	595494,5	4096742,6	-0,23	0,49	-0,16	0,28	-0,23	0,96
8	595406,89	4096729,21	0,07	0,18	0,00	0,09	-0,12	-0,04
9	594027,42	4096706,9	0,17	0,51	-0,22	0,34	0,06	0,12
10	592307,54	4096692,48	-0,11	-0,02	-0,06	0,08	-0,06	0,16
11	592229,01	4096831,51	0,23	-0,11	0,20	-0,17	0,17	-0,14

12	595570,94	4095148,65	-0,05	-0,05	0,09	-0,05	0,16	0,15
13	593924,05	4095109,99	-0,48	-0,40	-0,38	0,01	-0,48	-0,60
14	592201,41	4094754,63	-0,41	0,46	-0,09	0,38	-0,17	0,54
15	591581,53	4095387,22	0,19	0,26	0,07	0,26	0,37	0,62
16	591386,71	4095474,95	0,01	0,06	-0,04	-0,09	0,06	0,21
17	595389,69	4093290,39	0,26	0,26	0,38	0,32	0,32	0,38
18	593939,63	4093262,95	-0,26	0,27	-0,17	0,27	0,12	0,37
19	591828,22	4093270,46	-0,46	-0,28	-0,40	-0,22	-0,30	-0,22
20	591811,63	4093172,45	0,60	0,38	0,20	0,42	0,08	0,30
21	590625,15	4093229,84	-0,85	0,53	-0,74	0,59	-0,52	0,70
22	592663,35	4091993,05	0,46	0,45	0,22	0,51	0,40	0,03
23	592370,47	4092052,04	-0,22	0,01	0,00	-0,14	0,00	-0,10
24	592357,15	4092062,4	-0,09	0,26	-0,09	0,26	0,02	0,59
25	594197,98	4091451,92	0,16	0,16	0,12	0,23	0,12	0,12

Table 12: Measured coordinates for Pleiades 1B orthoimagery created from 3 bands data and compared with the one created using the Panchromatic data.

RESIDUALS			
ΔX			
	IHS 3	PCA 3	BROVEY 3
Check Pts	25	25	25
StDEV(m)	0,322	0,270	0,263
RMSE_X(m)	0,335	0,292	0,270
ΔY			
	IHS 3	PCA 3	BROVEY 3
Check Pts	25	25	25
StDEV (m)	0,279	0,262	0,362
RMSE_Y(m)	0,300	0,292	0,389

Table 13: Resulting residuals of the measured checkpoints

6.3. Panchromatic Data VS Four Band Data (RGB and NIR) and Three Band Data (RGB)

6.3.1. IHS Pansharpening

PANCHROMATIC		IHS (RGB)		IHS (RGB+NIR)		
A/A	X(m)	Y(m)	dX(m)	dY(m)	dX(m)	dY(m)
1	596781,08	4100183,16	-0,05	0,02	-0,03	-0,45
2	595844,45	4100188,55	-0,29	-0,25	-0,11	-0,23
3	595813,09	4098975,23	-0,55	0,07	-0,59	-0,23
4	594419,55	4099474,70	-0,27	-0,41	0,23	-0,20
5	595546,56	4098254,74	0,06	0,12	0,28	0,13
6	594187,43	4098554,90	-0,18	-0,25	-0,42	-0,27
7	595494,05	4096743,09	-0,23	0,49	0,37	0,45
8	595406,61	4096729,17	0,07	0,18	-0,12	-0,07
9	594026,79	4096706,20	0,17	0,51	0,52	0,29
10	592307,45	4096691,76	-0,11	-0,02	-0,20	0,25
11	592228,51	4096830,83	0,23	-0,11	0,02	-0,11

12	595570,29	4095148,80	-0,05	-0,05	0,35	0,15
13	593924,44	4095109,48	-0,48	-0,40	-0,95	1,37
14	593880,55	4095209,32	-0,41	0,46	-0,53	0,77
15	592201,03	4094754,67	0,19	0,26	0,15	0,24
16	591581,02	4095386,62	0,01	0,06	-0,14	0,10
17	591387,18	4095474,81	0,26	0,26	0,23	0,27
18	593940,32	4093262,39	-0,26	0,27	-0,48	0,55
19	591827,45	4093269,91	-0,46	-0,28	-0,26	-0,14
20	591811,12	4093172,25	0,60	0,38	0,02	0,21
21	590625,33	4093228,93	-0,85	0,53	-0,70	0,66
22	592663,46	4091993,31	0,46	0,45	0,17	0,34
23	592370,56	4092052,53	-0,22	0,01	-0,08	-0,36
24	592357,37	4092062,44	-0,09	0,26	0,00	0,34
25	594197,70	4091451,64	0,16	0,16	0,11	0,42

Table 14: Measured coordinates for Pleiades 1B orthoimagery created from Panchromatic data compared with measured coordinates on orthoimagery produced from 3band data (RGB) and 4 band data (RGB-NIR) created with IHS Pansharpening method.

RESIDUALS		
ΔX		
	IHS (RGB)	IHS (RGB+NIR)
Chck Pts	25	25
StDEV(m)	0,322	0,357
RMSE _X (m)	0,335	0,367
ΔY		
	IHS (RGB)	IHS (RGB+NIR)
Check Pts	25	25
StDEV (m)	0,279	0,399
RMSE _Y (m)	0,300	0,437

Table 15: Resulting residuals of the measured checkpoints

6.3.2. PCA Pansharpening

PANCHROMATIC		PCA (RGB)		PCA (RGB+NIR)		
A/A	X(m)	Y(m)	dX(m)	dY(m)	dX(m)	dY(m)
1	596781,08	4100183,16	-0,22	0,36	-0,17	-0,38
2	595844,45	4100188,55	-0,50	-0,20	0,20	-0,18
3	595813,09	4098975,23	-0,65	-0,03	-0,63	-0,01
4	594419,55	4099474,70	-0,06	-0,21	-0,11	-0,09
5	595546,56	4098254,74	0,06	0,35	0,16	0,23
6	594187,43	4098554,90	-0,36	-0,43	-0,47	-0,01
7	595494,05	4096743,09	-0,16	0,28	0,52	0,15
8	595406,61	4096729,17	0,00	0,09	-0,04	-0,08
9	594026,79	4096706,20	-0,22	0,34	-0,15	0,46
10	592307,45	4096691,76	-0,06	0,08	-0,16	-0,16
11	592228,51	4096830,83	0,20	-0,17	0,16	-0,21
12	595570,29	4095148,80	0,09	-0,05	0,41	0,29

13	593924,44	4095109,48	-0,38	0,01	-0,40	0,40
14	593880,55	4095209,32	-0,09	0,38	-0,98	1,27
15	592201,03	4094754,67	0,07	0,26	-0,08	0,09
16	591581,02	4095386,62	-0,04	-0,09	0,09	0,03
17	591387,18	4095474,81	0,38	0,32	0,30	0,03
18	593940,32	4093262,39	-0,17	0,27	-1,49	-0,42
19	591827,45	4093269,91	-0,40	-0,22	-0,38	-0,51
20	591811,12	4093172,25	0,20	0,42	0,09	0,22
21	590625,33	4093228,93	-0,74	0,59	-1,00	0,61
22	592663,46	4091993,31	0,22	0,51	0,20	0,28
23	592370,56	4092052,53	0,00	-0,14	-0,16	0,11
24	592357,37	4092062,44	-0,09	0,26	-0,09	0,28
25	594197,70	4091451,64	0,12	0,23	0,15	-0,12

Table 16: Measured coordinates for Pleiades 1B orthoimagery created from Panchromatic data compared with measured coordinates on orthoimagery produced from 3band data (RGB) and 4 band data (RGB-NIR) created with PCA Pansharpening method.

RESIDUALS		
ΔX		
	PCA (RGB)	PCA (RGB+NIR)
Chck Pts	25	25
StDEV(m)	0,270	0,460
RMSE_X(m)	0,292	0,487
ΔY		
	PCA (RGB)	PCA (RGB+NIR)
Check Pts	25	25
StDEV (m)	0,262	0,360
RMSE_Y(m)	0,292	0,372

Table 17: Resulting residuals of the measured checkpoints

6.3.3. Brovey Pansharpening

PANCHROMATIC		BROVEY (RGB)		BROVEY (RGB+NIR)		
A/A	X(m)	Y(m)	dX(m)	dY(m)	dX(m)	dY(m)
1	596781,08	4100183,16	-0,22	-0,16	-0,10	-0,16
2	595844,45	4100188,55	-0,39	-0,09	-0,29	-0,20
3	595813,09	4098975,23	-0,49	-0,09	-0,44	-0,03
4	594419,55	4099474,70	-0,27	-0,10	-0,69	0,00
5	595546,56	4098254,74	0,18	0,35	0,18	0,12
6	594187,43	4098554,90	-0,30	-0,49	-0,24	-0,37
7	595494,05	4096743,09	-0,23	0,96	0,58	1,56
8	595406,61	4096729,17	-0,12	-0,04	-0,15	-0,10
9	594026,79	4096706,20	0,06	0,12	0,11	0,29
10	592307,45	4096691,76	-0,06	0,16	0,17	0,42
11	592228,51	4096830,83	0,17	-0,14	0,27	0,08
12	595570,29	4095148,80	0,16	0,15	0,09	0,09
13	593924,44	4095109,48	-0,48	-0,60	-0,08	-0,10

14	593880,55	4095209,32	-0,17	0,54	-0,65	0,46
15	592201,03	4094754,67	0,37	0,62	-0,18	0,20
16	591581,02	4095386,62	0,06	0,21	-0,04	-0,09
17	591387,18	4095474,81	0,32	0,38	0,38	0,26
18	593940,32	4093262,39	0,12	0,37	-0,17	0,37
19	591827,45	4093269,91	-0,30	-0,22	-0,09	-0,12
20	591811,12	4093172,25	0,08	0,30	0,36	0,46
21	590625,33	4093228,93	-0,52	0,70	-0,63	0,48
22	592663,46	4091993,31	0,40	0,03	0,46	0,51
23	592370,56	4092052,53	0,00	-0,10	-0,11	-0,10
24	592357,37	4092062,44	0,02	0,59	0,24	0,59
25	594197,70	4091451,64	0,12	0,12	0,19	0,05

Table 18: Measured coordinates for Pleiades 1B orthoimagery created from Panchromatic data compared with measured coordinates on orthoimagery produced from 3band data (RGB) and 4 band data (RGB-NIR) created with Brovey Pansharpening method.

RESIDUALS		
ΔX		
	BROVEY (RGB)	BROVEY (RGB+NIR)
Check Pts	25	25
StDEV(m)	0,263	0,334
RMSE _x (m)	0,270	0,310
ΔY		
	BROVEY (RGB)	BROVEY (RGB+NIR)
Check Pts	25	25
StDEV (m)	0,362	0,380
RMSE _y (m)	0,389	0,414

Table 19: Resulting residuals of the measured checkpoints

6.4. Overall Evaluation

Table 20: Resulting residuals for all performed tests for Pleiades 1B dataset. presents the resulting residuals for all performed tests for Pleiades 1B dataset. More specifically, are presented the residuals of the comparison of the control dataset (VLSO) with the Panchromatic orthoimage, the orthoimages resulting from four band pansharpened data and three band pansharpened data. In addition, results of the comparison of the Panchromatic orthoimage with the orthoimages from pansharpened data of three and four bands are included.

RESIDUALS (m)					
PLEIADES 1B	RMSE _x	RMSE _y	RMSE _{xy}	AVERAGE	STDEV
VLSO-PAN	0,522	0,646	0,831	0,831	-
VLSO-IHS 4B	0,511	0,534	0,739		
VLSO-PCA 4B	0,567	0,539	0,782	0,788	0,052
VLSO-BROVEY 4B	0,517	0,666	0,843		
VLSO-IHS 3B	0,534	0,580	0,788		
VLSO-PCA 3B	0,580	0,570	0,813	0,815	0,028
VLSO-BROVEY 3B	0,544	0,645	0,844		

PAN-IHS 4B	0,367	0,437	0,571		
PAN-PCA 4B	0,487	0,372	0,613	0,567	0,048
PAN-BROVEY 4B	0,310	0,414	0,517		
PAN-IHS 3B	0,335	0,300	0,450		
PAN-PCA 3B	0,292	0,292	0,413	0,446	0,031
PAN-BROVEY 3B	0,270	0,389	0,474		

Table 20: Resulting residuals for all performed tests for Pleiades 1B dataset.

Since the accuracy comparison between the control dataset (VLSO) and the Pleiades 1B orthoimagery resulting from panchromatic data, has been already presented in paragraph 3.3, in this subsection is tried to be analyzed and interpreted the effect of pansharpener algorithms on the resulting orthoimagery.

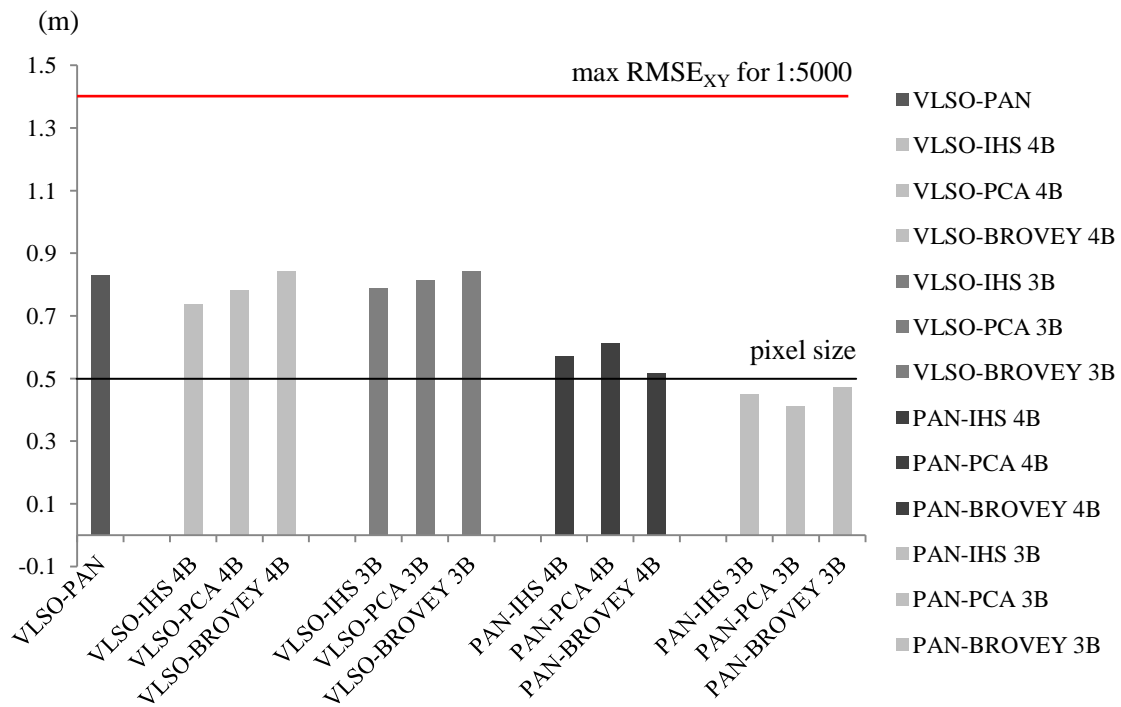


Figure 22: Graphic representation of Resulting residuals in meters

As it is observed, the orthoimagery from Panchromatic and Pansharpener data compared with the control dataset presents almost the same $RMSE_{XY}$ which equals to 0.810m in average, i.e. 1.60 times the pixel size of the GSD which is 0.50m. At the level of Pansharpener algorithms, it seems that systematically, the Brovey fusion appears with the largest residual errors, both in four band data (RGB-NIR) and three band data (RGB). However, the reported residuals are within the accuracy limits that are specified by the GRC Guidelines and NSSDA Accuracy Standards. Moreover, it is observed that orthoimagery resulting from four band data has almost the same residual errors as the orthoimagery produced from three band data.

For the comparison between the Panchromatic orthoimage and the orthoimages produced using Pansharpener data, it is obvious that the three band orthoimagery presents a better accuracy of 25%. This fact is not the expected since due to the existence of four bands, it was expected a more accurate DSM and thus a more accurate resulting orthoimage. However, the residual errors of both datasets are about at the size of the GSD and within the accuracy limits for producing LSO.

Between the pansharpening algorithms, the Brovey fusion has 75% frequency of presenting the largest residual errors and the PCA 25% frequency. The IHS pansharpening algorithm residual errors seem to be the most times similar with the average of the residual errors.

The above results suggest that the Pansharpening process does not affect the geometric accuracy of the resulting DSM of 10m interval and consequently the resulting orthoimagery. Moreover, differences between the orthoimages produced by DSMs from Pansharpened imagery were observed, they were not sufficient for affecting the overall accuracy of the orthoimages. To this end, DSMs could be generated either by panchromatic data either by pansharpened data as regards the tested algorithms without compromising the geometric accuracy of the produced orthoimage. This, leads the users to choose the appropriate fusion algorithm based only on its radiometric properties and capabilities.

6.5. Concluding Remarks

In Part I the accuracy and radiometric quality of orthorectified high resolution satellite imagery from Pleiades-1B and GeoEye-1 satellites were investigated through a comparative evaluation of their quantitative and qualitative properties with and LSO and a VLSO as the benchmark dataset. In addition, the advantages and limits of the Pleiades Imaging for producing Large Scale Orthophotos (LSO) were also investigated.

The performed visual assessment of the orthoimagery revealed that Pleiades 1B orthoimagery is especially promising presenting much more information and clearer forms. On the contrary, abrupt changes of brightness and contrast and high radiometric saturation levels were observed on the GeoEye-1 orthomosaic. The geometric evaluation reveals that the used LSO and Geoeye-1 orthomosaic suffer from a systematic error in Y axis. In addition, Pleiades 1B and LSO imagery have almost the same absolute accuracy.

Both radiometric and accuracy test results show that Pleiades 1B orthoimage has almost the same absolute accuracy as the orthomosaic from aerial imagery (LSO from Hellenic National Cadastre & Mapping Agency S.A.). Hence, it could easily replace aerial imagery, when it comes to orthoimage production. Furthermore, all data are adequate for producing LSO for mapping and GIS, according to JRC, ASPRS and NSSDA accuracy standards. The results also serve for a critical approach for the usability and cost efficiency of satellite imagery for the production of LSO.

In Part II the effects of the IHS, PCA and Brovey pansharpening algorithms on resulting orthoimagery were presented. To this direction, an iterative methodology was applied in order to combine the methodology described in CHAPTER 2. DSMs and Orthoimages were created using only the Panchromatic and the Pansharpened data for each block. In this way, for each different block, the same control points, check points and tie points were used.

Results demonstrated that DSMs could be generated either by panchromatic data or by pansharpened data as regards the tested algorithms without compromising the geometric accuracy of the produced orthoimage.

6.6. Future Work

Future work includes testing more state of the art pansharpening algorithms on more Very High Resolution Satellite imagery such as GeoEye-1 and WorldView-2. In addition, these tests will be applied using various software and freeware in order to acquire more reliable and objective results for this investigation.

References

- Abdullah, Q. A., & Answered, Y. Q. (2008). Mapping matters.
- Abdullah, Q. A., & Answered, Y. Q. (2013). Mapping matters.
- Aguilar, M. A., Agüera, F., Aguilar, F. J., and Carvajal, F., 2008. Geometric accuracy assessment of the orthorectification process from very high resolution satellite imagery for Common Agricultural Policy purposes. *International journal of remote sensing*, 29(24), pp. 7181-7197.
- Aiazzi, B., Alparone, L., Baronti, S., Garzelli, A., and Selva, M., “Twenty- five years of pansharpening: A critical review and new developments,” in *Signal and Image Processing for Remote Sensing*, C.-H. Chen, Ed., 2nd ed. Boca Raton, FL, USA: CRC Press, 2012, pp. 533–548
- Amolins, L., Zhang, Y., and P. Dare, “Wavelet based image fusion techniques-An introduction, review and comparison,” *ISPRS J. Photogramm. Remote Sens.*, vol. 62, no. 4, pp. 249–263, Sep. 2007.
- Amro, I., Mateos, J., Vega, M., Molina, R., & Katsaggelos, A. K. (2011). A survey of classical methods and new trends in pansharpening of multispectral images. *EURASIP J. Adv. Sig. Proc.*, 2011, 79.
- Astrium, 2012. Pléiades Imagery User Guide. October 2012-v2.0.
- Burt P. J. and Adelson E. H, “The Laplacian pyramid as a compact image code,” *IEEE Trans. Commun.*, vol. COM-31, no. 4, pp. 532–540, Apr. 1983.
- Carper, W. J., Lillesand, T. M., and Kiefer, P. W., The use of intensity-hue-saturation transformations for merging spot panchromatic and multispectral image data, *Photogramm. Eng. Remote Sens.*, vol. 56, no. 4, pp. 459–467.
- Chavez, P. and Howell, J., 1988. “Comparison of the spectral information content of Landsat thematic mapper and spot for three different sites in the Phoenix, Arizona region,” *Photogramm. Eng. Remote Sens.*, vol. 54, no. 12, pp. 1699-1708.
- Chavez, P. S., Kwarteng, Jr. and A. W., “Extracting spectral contrast in Landsat Thematic Mapper image data using selective principal component analysis,” *Photogramm. Eng. Remote Sens.*, vol. 55, no. 3, pp. 339–348, Mar. 1989.
- Cheng, Ph., Chaapel, C., 2008. Using WorldView-1 stereo data with or without ground control points. *GEOinformatics* 11 (7), pp. 34–39.
- Crespi, M., and De Vendictis, L., 2009. A procedure for high resolution satellite imagery quality assessment. *Sensors*, 9(5), pp. 3289-3313.

- Edwards, K. and Davis, P., 1994. The use of intensity-hue-saturation transformation for producing color shaded relief images, *Photogramm. Eng. Remote Sens.*, vol. 60, no. 11, pp. 1369–1373.
- Eisenbeiss, H., Baltsavias, E., Pateraki, M., and Zhang, L., 2004. Potential of IKONOS and QUICKBIRD imagery for accurate 3D-Point positioning, orthoimage and DSM generation. *International Archives of the Photogrammetry, Remote Sensing and Spatial Information Sciences*, 35(B3), pp. 522-528.
- Fasbender, D., Radoux, J., and Bogaert, P., “Bayesian data fusion for adaptable image pansharpening,” *IEEE Trans. Geosci. Remote Sens.*, vol. 46, no. 6, pp. 1847–1857, Jun. 2008.
- FGDC. 1998. Geospatial Positioning Accuracy Standards Part 3: National Standard for Spatial Data Accuracy, FGDC-STD-007.3-1998 https://www.fgdc.gov/standards/projects/FGDC-standards-projects/accuracy/part3/index_html
- Fraser, C.S., E. Baltsavias and A. Gruen (2002): Processing of Ikonos imagery for submetre 3D positioning and building extraction, *ISPRS J. Photogramm. Remote Sensing*, 56, 177-194
- Gary A Shaw and Hsiao-hua K Burke, “Spectral imaging for remote sensing,” *Lincoln Laboratory Journal*, vol. 14, no. 1, pp. 3–28, 2003
- Gleyzes, M. A., Perret, L., and Kubik, P., 2012. Pleiades system architecture and main performances. *International Archives of the Photogrammetry, Remote Sensing and Spatial Information Sciences*, 39, B1.
- Gonzalez, R.C., Woods, R.E., *Digital image processing*, 3rd edn. (Prentice Hall,2008)
- Greenfeld, J., 2001. Evaluating the accuracy of Digital Orthophoto Quadrangles (DOQ) in the context of parcel-based GIS. *Photogrammetric engineering and remote sensing*, 67(2), pp. 199-206.
- Haydn, R., Dalke, G. W., Henkel, J., and Bare, J. E., 1982. Application of the IHS color transform to the processing of multisensor data and image enhancement. In *Proceedings of the International Symposium on Remote Sensing of Environment, First Thematic Conference: "Remote sensing of arid and semi-arid lands"*, Cairo, Egypt.
- Helder, D., Choi, J., 2003. On-orbit Modulation Transfer Function (MTF) measurements on QuickBird. In: *Proceedings of the 2003 High Spatial Resolution Commercial Imagery Workshop, NASA/NIMA/USGS Joint Agency Commercial Imagery Evaluation Team: Reston, VA, USA.*
- Ioannidis, C., and Katsigiannis, A., 2006. Accuracy comparison tests on ortho-rectified high resolution satellite images. *Revue française de photogrammétrie et de télédétection*, (184), 95-100.
- Ioannou, M. T., and Georgopoulos, A., 2013. Evaluating large scale orthophotos derived from high resolution satellite imagery. In *First International Conference on*

Remote Sensing and Geoinformation of Environment. International Society for Optics and Photonics, pp. 879515-879515.

Jacobsen, K., 2011. Characteristics of very high resolution optical satellites for topographic mapping. *International Archives of the Photogrammetry, Remote Sensing and Spatial Information Sciences*, XXXVIII (4/W19), on CDROM.

Kapnias, D., Milenov, P., and Kay, S. 2008. Guidelines for Best practice and quality checking of ortho imagery. Joint Research Centre, (3.0).

Kohm, K., 2004. Modulation transfer function measurement method and results for the OrbView-3 high resolution imaging satellite. *International Archives of the Photogrammetry, Remote Sensing and Spatial Information Sciences*, 35 (B1), pp. 7–12.

Laben C. A. and Brower B. V., “Process for enhancing the spatial resolution of multispectral imagery using pan-sharpening,” U.S. Patent 6 011 875, 2000, Eastman Kodak Company, Tech. Rep.

Leger, D., Viallefont, F., Deliot, P., Valorge, C., 2004. On-orbit MTF assessment of satellite cameras. In: Morain, S.A., Budge, A.M. (Eds.), *Post-Launch Calibration of Satellite Sensors*. Taylor and Francis Group, London, UK, pp. 67–76.

Li, S. and Yang, B., “A new pan-sharpening method using a compressed sensing technique,” *IEEE Trans. Geosci. Remote Sens.*, vol. 49, no. 2, pp. 738–746, Feb. 2011.

Niu, X., Wang, J., Di, K., Lee, J-D., Li R., 2004. Geometric modelling and photogrammetric processing of high-resolution satellite imagery. In: *The International Archives of the Photogrammetry, Remote Sensing and Spatial Information Sciences*, Istanbul, Turkey, Vol. XXXV, Part B4, pp. 689-694.

Padwick, C., Deskevich, M. I. C. H. A. E. L., Pacifici, F., and Smallwood, S., 2010. WorldView-2 pan-sharpening. *Proc. American Society for Photogrammetry and Remote Sensing*, 13.

Palsson, F., *Pansharpening and Classification of Pansharpened Images*, June 2013, <http://skemman.is/handle/1946/15664>

Palsson, F., Sveinsson, J. R., and Ulfarsson, M. O., “A new pansharpening algorithm based on total variation,” *IEEE Geosci. Remote Sens. Lett.*, vol. 11, no. 1, pp. 318–322, Jan. 2014.

Palsson, F., Sveinsson, J. R., Benediktsson, J. A., & Aanaes, H. (2012). Classification of pansharpened urban satellite images. *Selected Topics in Applied Earth Observations and Remote Sensing, IEEE Journal of*, 5(1), 281-297.

Palsson, F., Sveinsson, J. R., Benediktsson, J. A., and Aanaes, H., 2012. Classification of pansharpened urban satellite images. *Selected Topics in Applied Earth Observations and Remote Sensing, IEEE Journal of*, 5(1), pp. 281-297.

- Pohl, C., Van Genderen, J.L., “Multisensor image fusion in remote sensing: concepts, methods and application”, *International Journal of Remote Sensing*, vol. 99, no. 5, pp. 823-854, 1998.
- Poli, D., Remondino, F., Angiuli, E., and Agugiaro, G., 2014. Radiometric and geometric evaluation of GeoEye-1, WorldView-2 and Pléiades-1A stereo images for 3D information extraction. *ISPRS Journal of Photogrammetry and Remote Sensing*.
- Shah, V. P., Younan, N. H., and King, R. L., “An efficient pan-sharpening method via a combined adaptive-PCA approach and contourlets,” *IEEE Trans. Geosci. Remote Sens.*, vol. 46, no. 5, pp. 1323–1335, May 2008.
- Thomas, C., Ranchin, T., Wald, L., and Chanussot, J., “Synthesis of multispectral images to high spatial resolution: A critical review of fusion methods based on remote sensing physics,” *IEEE Trans. Geosci. Remote Sens.*, vol. 46, no. 5, pp. 1301–1312, May 2008.
- Tu, T. M., Huang, P. S., Hung, C. L., and Chang, C. P., 2004. A fast intensity-hue-saturation fusion technique with spectral adjustment for IKONOS imagery. *Geoscience and Remote Sensing Letters, IEEE*, 1(4), pp. 309-312.
- Vijayaraj, V., O'Hara, C.G., Younan, N.H., Quality analysis of pansharpened images. *Proc IEEE Int Geosc Remote Sens Symp IGARSS '04* 1, 20–24 (2004)
- Xu, F. and Woodhouse, N. and Xu, Z. and Marr, D. and Yang, X. and Wang, Y., 2008. Blunder elimination techniques in adaptive automatic terrain extraction. *ISPRS J.*, 29 (3), 21. p.1139-1148.
- Zhou, G., Li, R., 2000. Accuracy evaluation of ground points from IKONOS high-resolution satellite imagery. *Photogrammetric Engineering and Remote Sensing*, 66(9), pp. 1103-1112.
- Zhu, X. X. and Bamler, R., “A sparse image fusion algorithm with application to pan-sharpening,” *IEEE Trans. Geosci. Remote Sens.*, vol. 51, no. 5, pp. 2827–2836, May 2013.

Appendix I

Essential Statistics Review

In most experiments that include repetitive measurements of the same variable, when performed carefully, there is a certain expectancy of the outcome of the measurement.

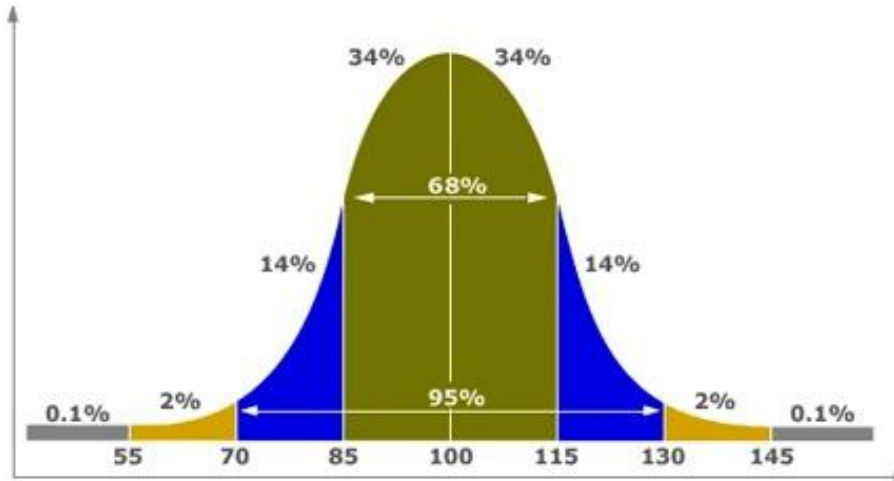


Figure 23: The normal distribution curve showing a typical bell shape curve (modified from <http://theeducationsociety.com/tag/bell-curve/>).

The random, yet clustered, distribution is the normal distribution of the natural occurrence of things in nature. If we plot the results of the 100 outcomes of the experiment, it will result in the well-known bell-shape curve (see Figure 2).

The concept of normal distribution is important in science, as the question always arises as to what makes the new findings or results trustworthy or significant. In statistics, when we talk about the significance of the results we use the unit of significance or standard deviation (σ). The standard deviation, or sigma, measures the disparity of the result or error (as we are always concerned about measuring the errors in lidar data) from the mean value of such errors. Let us now try to understand such a statement in terms of the normal distribution curve (Figure 2).

In Figure 1, there is always a chance that 68% of the errors will fall within the standard deviation value of $\pm 1\sigma$ (between $-\sigma$ and $+\sigma$). In other words, if the project specification calls for lidar data with an accuracy of one sigma equal to 15 cm and the client tested the accuracy of the data with 20 ground checkpoints, then the client should find 68% or more of the individual error values from the 20 points fall within 15 cm, with a possibility that 32% of the checkpoints will have an error in excess of 15 cm. Similarly, there is a chance that 95% of the individual error values fall within $\pm 2\sigma$ or 30 cm.

$$StDEV = \sqrt{\frac{\sum d^2}{n-1}} \quad (1)$$

$$RMSE_X = \sqrt{\sum_{i=1}^n (X_{data} - X_{check})^2} \quad (2)$$

$$RMSE_Y = \sqrt{\sum_{i=1}^n (Y_{data} - Y_{check})^2} \quad (3)$$

$$RMSE_{XY} = \sqrt{(RMSE_X)^2 - (RMSE_Y)^2} \quad (4)$$

where d = the deviation
 n = the number of check points
 X, Y_{check} = the check points coordinates measured on control dataset and
 X, Y_{data} = the points coordinates measured on test dataset

The standard deviation, or sigma, is an indicator of how well the measurements fit each other. An individual error with a value of 3σ indicates that such a point does not fit the model properly, as it is far from the mean and so on. A large sigma value indicates that the individual errors fluctuate widely around the mean, while smaller sigma values mean the errors are close to each other as well as the mean. This conclusion can also be derived by looking at the bell curve. A flattened bell curve shape indicates widely dispersed errors around the mean, while a narrow bell shape indicates a close proximity of the errors to each other and the mean. The Standard Deviation expresses how far an individual error is from the mean (Abdullah, 2013).

Appendix II

Paper

This paper is published in "The International Archives of the Photogrammetry, Remote Sensing and Spatial Information Sciences" Volume: XL-3/W2 and presented in the context of "Photogrammetric Image Analysis" (PIA) and "High Resolution Earth Imaging for Geospatial Information (HRIGI)" - Joint ISPRS conference 2015, 25–27 March 2015, Munich, Germany

URL : <http://www.int-arch-photogramm-remote-sens-spatial-inf-sci.net/XL-3-W2/1/2015/isprsarchives-XL-3-W2-1-2015.html>

COMPARATIVE ASSESSMENT OF VERY HIGH RESOLUTION SATELLITE AND AERIAL ORTHOIMAGERY

P. Agrafiotis, A. Georgopoulos

National Technical University of Athens, School of Rural and Surveying Engineering, Lab. of Photogrammetry
Zografou Campus, Heron Polytechniou 9, 15780, Zografou, Athens, Greece
(pagraf, drag)@central.ntua.gr

Commission I, WG I/4

KEY WORDS: Pleiades, Accuracy, Radiometry, Orthoimage, Statistical Analysis

ABSTRACT:

This paper aims to assess the accuracy and radiometric quality of orthorectified high resolution satellite imagery from Pleiades-1B satellites through a comparative evaluation of their quantitative and qualitative properties. A Pleiades-B1 stereopair of high resolution images taken in 2013, two adjacent GeoEye-1 stereopairs from 2011 and aerial orthomosaic (LSO) provided by NCMA S.A (Hellenic Cadastre) from 2007 have been used for the comparison tests. As control dataset orthomosaic from aerial imagery provided also by NCMA S.A (0.25m GSD) from 2012 was selected. The process for DSM and orthoimage production was performed using commercial digital photogrammetric workstations. The two resulting orthoimages and the aerial orthomosaic (LSO) were relatively and absolutely evaluated for their quantitative and qualitative properties. Test measurements were performed using the same check points in order to establish their accuracy both as far as the single point coordinates as well as their distances are concerned. Check points were distributed according to JRC Guidelines for Best Practice and Quality Checking of Ortho Imagery and NSSDA standards while areas with different terrain relief and land cover were also included. The tests performed were based also on JRC and NSSDA accuracy standards. Finally, tests were carried out in order to assess the radiometric quality of the orthoimagery. The results are presented with a statistical analysis and they are evaluated in order to present the merits and demerits of the imaging sensors involved for orthoimage production. The results also serve for a critical approach for the usability and cost efficiency of satellite imagery for the production of Large Scale Orthophotos.

1. INTRODUCTION

As satellite optical sensor technology progresses, very high resolution (VHR) images from space become available and lucrative for large scale mapping. Resolutions of less than 1m reaching the level of a few tens of centimetres are common today thus enabling the users to distinguish fine detail on the earth's surface, like buildings, individual trees and even smaller objects. For applications concerned with mapping, cadastral recording and land monitoring VHR satellite imagery is directly challenging conventional or even digital aerial images of comparable resolution

1.1 Motivation

The Pléiades 1B are a very high-resolution satellite constellation delivering 50-cm Ortho products as a standard (Astrium, 2012). In the context of the Pleiades evaluation program, the Laboratory of Photogrammetry of National Technical University of Athens acquired a triplet of high resolution images taken in 2013 by Pleiades 1B over the small Cyclades island of Antiparos in order to assess their usability and accuracy and compare it to similar satellite sensors. In the literature, the radiometric characteristics and the geometric accuracy of optical sensors and their resulting imagery have been extensively addressed in various contribution (Zhou and Li, 2000; Greenfeld, 2001; Niu et al., 2004; Eisenbeiss et al., 2004; Ioannidis and Katsigiannis, 2006; Cheng and Chaapel, 2008; Aguilar et al., 2008; Crespi and De Vendictis, 2009; Jacobsen, 2011). However, these contributions do not perform any comparative evaluation on the quantitative and qualitative

properties of the resulting orthoimagery exploiting aerial Large Scale Orthophotos and Very Large Scale Orthophotos.

This paper aims to report the assessment of the accuracy and radiometric quality of orthorectified high resolution satellite imagery from Pleiades-1B satellites through a comparative evaluation of their quantitative and qualitative properties. In addition, the advantages and limits of the Pleiades Imaging for producing Large Scale Orthophotos (LSO) are investigated.

2. DATASETS

A Pleiades 1B stereopair of high resolution images taken in 2013 (0.50m GSD), two adjacent GeoEye-1 stereopairs (0.50m GSD) acquired for a diploma thesis (Ioannou and Georgopoulos, 2013) from which a high resolution orthomosaic had already been produced and aerial LSO (0.50m GSD) provided by the Hellenic National Cadastre & Mapping Agency S.A. (NCMA S.A) from 2007 have been used for the comparison tests. As control dataset aerial orthomosaic (VLSO) was also provided also from NCMA S.A with 0.25m GSD from 2012.

The study area, the small Cycladic island of Antiparos has an area of 35000 km² and it is very close to Paros island. It measures 12.5 km in length and 5.5 km in width and has a coastal perimeter of 54 km. Even though the island is almost flat, a few little hills in the centre reach a maximum height of 300 metres. The landscape is rather wild and varied including a main settlement and agricultural fields. Finally, on the west coast there are steep cliffs.

2.1 Test Dataset

2.1.1 The Pleiades 1B Imagery: As already mentioned, the Pleiades twins are very high-resolution satellites delivering 50cm Ortho products as a standard (Astrium, 2012). Pleiades-1B satellite sensor was successfully launched on December 2, 2012. Built by AIRBUS Defence & Space, the satellite was launched from a Soyuz launcher at the European Space Centre in French Guiana. Pleiades-1A and 1B satellites will be phased 180° apart in the same near-polar sun-synchronous orbit at an altitude of 694 km, enabling daily revisits to any location on the planet. The sensor can reach a ground resolution of 0.7m in panchromatic mode and 2.8m in multi-spectral mode in vertical direction. The images provided for this work were acquired in the tri-stereo mode for 3D information. According to this acquisition scheme, the satellite rotates around its axis and the HiRi camera scans a target area from three different viewing directions during one pass, thus resulting in a triplet (Gleyzes et al., 2012). However, for reasons of objectivity in comparison with data from GeoEye-1, only the 2 external images of the tri-stereo were used. The images were acquired on 9 April 2013 in the morning within 22.5 seconds. The average viewing angles of the two selected images are, respectively, 6.30° and 9.47° in across-track direction with respect to the nadir and 1.63° and -12.39° in across-track direction (Figure 1).

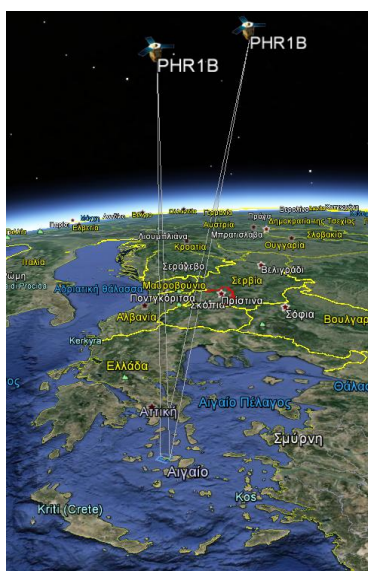


Figure 1. Stereo acquisition for 3D applications (Google Earth preview of the footprints and the satellite's position)

2.1.2 The GeoEye-1 Imagery: Geoeeye-1 satellite was launched in September 2008. The sensor's vertical ground resolution of 0.41m for panchromatic imagery and 1.65 m for the 4-band multispectral imagery is resampled to 0.50 m and 2.00 m, respectively for commercial customers. The Geoeeye-1 sensor was designed mainly for commercial use, with Google as one of its most valued customers. They use the imagery for their Google Maps and Google Earth applications. Geoeeye Inc. markets this imagery by offering three basic product packages, which are distinguished by the level of positional accuracy they produce.

For the purposes of this study, two adjacent Geoeeye-1 stereopairs from December 2011 were used. These high resolution stereopairs were collected in the same orbital pass, thus minimizing changes in lighting or scene content. They are accompanied by an RPC camera model file for georeferencing.

The images were collected during the single orbital pass and they consist of an image collected at a low elevation angle of above 60 degrees as well as an image collected at a high elevation angle of above 72 degrees. Choices of projection, including epipolar projections for stereo applications are also provided. The data consists of 8 or 11 bits per pixel imagery and is provided in GeoTIFF format, including metadata files.

2.1.3 The Aerial Imagery Orthomosaic (LSO): The tested LSO provided by NCMA S.A had 0.50m GSD and the imagery were taken on 2007. This dataset has a geometric accuracy of RMSE_{xy} ≤ 1.41m (95% confidence level).

2.2 Control Dataset

In order to evaluate the produced orthoimages, accuracy specifications had to be set as a reference for the purpose of inferring about the actual metric efficiency of the product. As control dataset aerial imagery orthomosaic (VLSO) provided by Hellenic National Cadastre & Mapping Agency S.A. (NCMA S.A) was used. It had 0.25m GSD and the imagery was taken on August 12th 2012. According to NCMA S.A. the orthomosaic of the control dataset was created from aerial imagery of a scale of 1:15000 using a ZEISS RMK TOP 30 film camera having a lens of 153.12mm. To produce this orthoimagery, a DEM was created having 5m grid interval.

3. METHODOLOGY

The methodology applied in this paper follows the well-known photogrammetric procedures in order to compare and assess the radiometric and geometric performance of very high resolution imagery from Pleiades 1B and GeoEye-1 and aerial orthoimagery. Main goal of the methodology is to deliver reliable and objective results through a statistical analysis of the metric results exploiting commonly accepted standards for accuracy testing of orthoimages.

3.1 GCP measurements and Distribution

A number of ground control points were determined by GPS observations, which were suitably post-processed in order to get accurate measurements (mean uncertainty of 0.010m), distributed all over the area of interest. Some of these points have been used for the determination of orientation parameters as GCPs, and the rest as check points.

3.2 Pansharpening

The three stereopairs, 2 for GeoEye-1 which contain the northern and southern regions of the island of Antiparos and one for Pleiades 1B containing the whole island, included 5 bands; one panchromatic with a GSD of 0.50 m and four multispectral (R, B, G and NIR) with a GSD of 2.00 m. For this study, only the three multispectral bands Red, Green and Blue were necessary.

Thus, pansharpening procedures took place in order to enable the further photogrammetric processing of the imagery. Various algorithms were tested in order to achieve the optimal visual result, including the Principal Component Analysis technique, the IHS (Intensity-Hue-Saturation), the Brovey fusion and the HCS (Hyperspherical Color Space) Resolution Merge. From these tests, the algorithm HCS Resolution Merge proved to yield the most acceptable visual results for the available Geoeeye-1 stereo pairs and the algorithm IHS for Pleiades 1B stereopair.

3.2.1 IHS for Pleiades 1B Data: A high-resolution colorized product from Pleiades 1B data was produced by using the IHS pan-sharpening algorithm. The Intensity-Hue-Saturation (IHS) method (Haydn et al., 1982) has been widely used (Carper et al., 1990, Chavez and J. Bowell, 1988, Edwards and P. Davis 1994, Tu et al., 2004) for pansharpening satellite images. In this frequently used method, a component derived from the MS image is substituted for a component derived from the PAN image and then the fused or pansharpened image is obtained from the inverse transformation. The basic idea is to first transform the MS image into intensity (I), hue (H) and saturation (S) components (IHS colour space). The next step is to adjust the Pan image so that it has the same mean and variance as the intensity component of the MS image. The intensity component is then replaced with the appropriately scaled Pan image and finally the inverse IHS transformation is taken to get the fused image. The IHS method produces images that have high spatial resolution and low spectral quality (Palsson et al., 2012).

3.2.2 HCS for GeoEye-1 Data: Hyperspherical Color Space (HCS) pan-sharpening (Padwick et al, 2010) is an algorithm especially designed for processing images captured by the Worldview-2 satellite, which supports an 8 band multispectral and panchromatic sensor. The main concept of the algorithm is a transformation from the local color space to the hyperspherical color space. The multispectral RGB data are redefined by its band components into angular variables (ϕ_1 , ϕ_2 , ϕ_3) which describe the color or hue, and a radial component (I) which defines the intensity of the color in hyperspherical space. The naïve approach of the algorithm simply replaces the multispectral intensity component with an intensity matched version of the panchromatic band using the normalized mean and standard deviation of the hyperspherical data. This is followed by a reverse transformation into the RGB color space for the compilation of the pan-sharpened image (Padwick et al, 2010). The technique is applicable to images composed of at least three bands and ideal for those with a great number of bands, such as Worldview-2, but the results were more than satisfactory for the Geoeye-1 RGB image of this project.

3.3 Photogrammetric Georeference

The photogrammetric georeference was performed using the commercial software LPS and Photomod. To this direction, after a 1st degree polynomial Rational Polynomial Coefficients (RPC) refinement, tie points and ground control points (GCPs) were measured on the images. 4 GCPs and 6 checkpoints were used for Pleiades 1B data achieving a RMSE of 0.045m while 5 GCPs and 10 checkpoints were used for GeoEye-1 data achieving a RMSE of 0.160m.



Figure 2. Ground control points and check points used for Pleiades 1B data

The occurred deviation between the RMSE of Pleiades 1B and GeoEye-1 data is justified by the increased radiometric saturation of GeoEye-1 imagery and is discussed further in Section 4.1. At this point it is noted that on the Pleiades 1B data less GCPs and checkpoints were measured because of the clouds on the lower right corner of the imagery.

3.4 DEM Extraction and Orthoimage Production

For the DSM extraction, an automatic procedure was applied for Pleiades 1B while a semi-automatic one was applied for the Geoeye-1 stereopair. The semi-automatic procedure was implemented because of problems occurring on coastal and rocky areas presenting steep terrain. In addition, GCPs were used for transferring the scale and real elevation values while the grid interval was selected as 10 m.

As regards the production of the orthoimages (Figure 3,4), they were created using bilinear interpolation. A GSD of 0.50m was selected while it should be mentioned that the orthorectification of all images of the stereopairs was performed in order to check the DSM for gross errors by subtracting them.



Figure 3. Pleiades 1B orthoimage



Figure 4. GeoEye-1 orthomosaic

4. QUALITY AND ACCURACY ASSESSMENT

The results are presented with a statistical analysis and they are evaluated in order to present the merits and demerits of the imaging sensors involved. To this direction the Standard Deviation (σ) or sigma are computed as an indicator of how well the measurements fit to each other and as a measure of precision. In addition, the Root Mean Square Error (RMSE) is computed for Northing and Easting coordinates. As observed, in aerial LSO and Geoeye-1 orthomosaic, the Standard Deviation and $RMSE_{X,Y}$ differ, indicating a systematic error in Y axis. Thus, a bias removal procedure was applied in order to evaluate orthoimages objectively and accurately.

4.1 Image Quality Assessment

The radiometry of an image is satisfactory when the relationship between the ground reflectance of the target and the grey level of the pixel on the image is correct (Crespi and De Vendictis, 2009). Pleiades 1B and GeoEye-1 sensors provide images with radiometric resolution of 12 bit/pixel. Thus, a higher dynamic range and signal-to-noise ratio with respect to traditional scanned 8-bit/pixel images is expected (Poli et al., 2014).

4.1.1 Visual Assessment: Visual inspection of the orthoimages was applied in order to identify errors and/or image defects. As an example, in GeoEye-1 images some abrupt changes of brightness and contrast were observed. In addition, many regions presented extremely dark/light tones, predominantly on the buildings and along the roads.

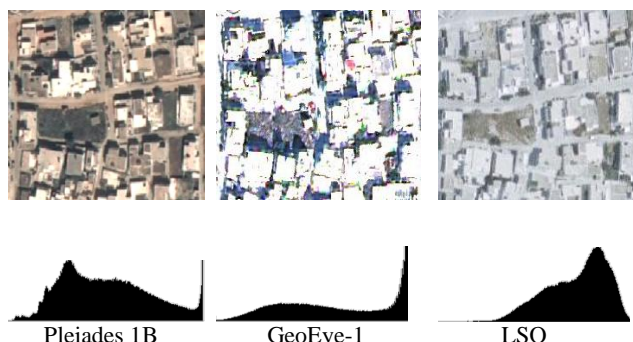


Figure 5. Examples of visual errors/defects of the orthoimages and their corresponding histograms

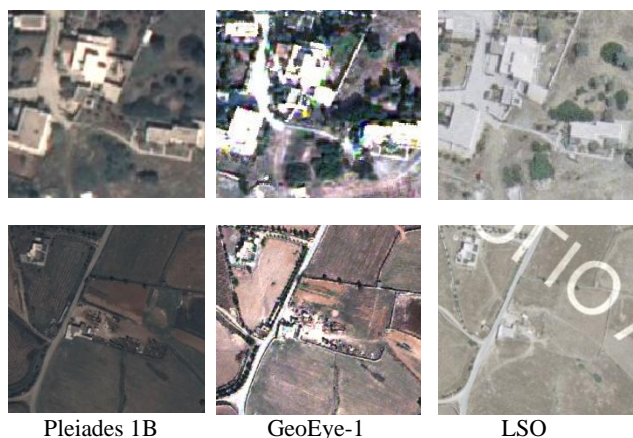


Figure 6. Examples of visual errors/defects of the orthoimages

Contrary, in Pleiades 1B image, the radiometric saturation of certain regions is especially prominent presenting much more information and clearer forms (Figure 5, 6). Moreover, the orthoimage resulting from Pleiades 1B imagery is much darker than LSO and Geoeye-1 imagery. Important radiometric changes between two or more images are critical during automatic homologue point identification and during image correlation thus causing mismatches and wrong height estimation (Poli et al., 2014).

Histograms are the basis for numerous image processing techniques. In addition, histograms provide useful image statistics. In a dark image, the components of the histogram are concentrated on the lower side of the intensity scale while these components of a light image are biased toward the higher side of the scale. The histogram of a low contrast image has a limited range while on a high contrast image the components of the histogram cover a wide range of the intensity scale (Gonzalez and Woods, 2002). In figure 5, histograms of the presented part of the study area, indicates that LS Orthomosaic is characterized by low contrast and high luminosity. However, GeoEye-1 orthomosaic presents higher luminosity than LS Orthomosaic and very high frequency of tones near the white (255). Pleiades 1B orthoimagery presents a more normalized histogram with a wide range and components concentrated near the low side of the scale, indicating a darker image.

In addition to visual inspection of the images, the noise level and the geometrical resolution and sharpness which is described by the Modulation Transfer Function (MTF) are encountered in the literature. By the term noise the non-homogeneities in the image are described and it is evaluated on non-homogeneous areas. Over these areas, the noise variation is considered as function of intensity. It should be noted that noise for CCD-images is not additive but intensity-dependent (Poli et al., 2014). The Modulation Transfer Function (MTF) is used to estimate the spatial performance of an imaging sensor. In case of on-orbit MTF estimation, the edge method is generally used (Helder and Choi, 2003; Kohm, 2004; Leger et al., 2004; Crespi and De Vendictis, 2009, Poli et al., 2014).

4.2 Spatial Accuracy assessment

The two resulting orthoimages and the aerial imagery orthophoto (LSO) were evaluated relatively and absolutely for their quantitative and qualitative properties. Check points were measured on the VLISO product and test measurements were performed using the same check points in order to establish their accuracy both as far as the single point coordinates as well as their distances were concerned. 26 Check Points for Pleiades 1B and 26 Check Points for Geoeye-1 and LSO were distributed in total according to JRC Guidelines for Best Practice and Quality Checking of Ortho Imagery (Kapnias et al., 2008) and National Standard for Spatial Data Accuracy (NSSDA) (FGDC, 1998) standards while areas with different terrain relief and land cover were also included. Performed tests were also based on JRC and NSSDA accuracy standards.

4.2.1 The National Standard for Spatial Data Accuracy (NSSDA): The NSSDA implements a statistical and testing methodology for estimating the positional accuracy of points on maps and in digital geospatial data, with respect to georeferenced ground positions of higher accuracy. The NSSDA applies to georeferenced maps and digital geospatial data, in either raster, point, or vector format (FGDC, 1998).

The NSSDA does not define threshold accuracy values and uses the root-mean-square error (RMSE) to estimate positional accuracy.

4.2.2 JRC Guidelines for Best Practice and Quality Checking of Ortho: These guidelines apply to digital orthoimagery products, generated from either film cameras or digital sensors, on both airborne or satellite platforms for the scope of applications requiring accuracy of 0.5m-10m pixel size and large scale mapping or cadastre applications (0.5m or better). All stages of the production chain affecting geometric accuracy and radiometric quality of the final product are considered (Kapnias et al., 2008). As with the NSSDA procedure, the final orthoimage is assessed using the RMSE_x and RMSE_y and the associated DEM from RMSE_z. The use of RMSE provides a straight forward global statistic for assessing the final geometric accuracy. Additional indices such as the mean error and the error standard deviation can be used in order to better describe the spatial variation of errors or to identify potential systematic discrepancies.

4.2.3 Checkpoints Selection and Distribution: According to the NSSDA and JRC Guidelines, accuracy testing should be performed using an independent source of higher positional accuracy. The accuracy of the independent test points should fall within one-third of the intended accuracy (95% confidence level) of the examined dataset. A minimum of 20 well defined test points should be used to evaluate the accuracy of the dataset. The check points will be ideally evenly distributed and located across the image (Figure 6). The selected check point positions may be located with reference to the positions of the GCPs used to correct the imagery in order to ensure that the two sets of points are independent (CPs should not be close to the GCPs).

The location or the distribution of the checkpoints is also specified in NSSDA and JRC guidelines. These Standards assume that the area to be evaluated is a rectangle and is divided into four quads and a diagonal is to be established across the area. At least 20% of the points should lie in each quarter whereas the optimum distance between points (is related to the diagonal distance of the area (1/10th of the diagonal length).

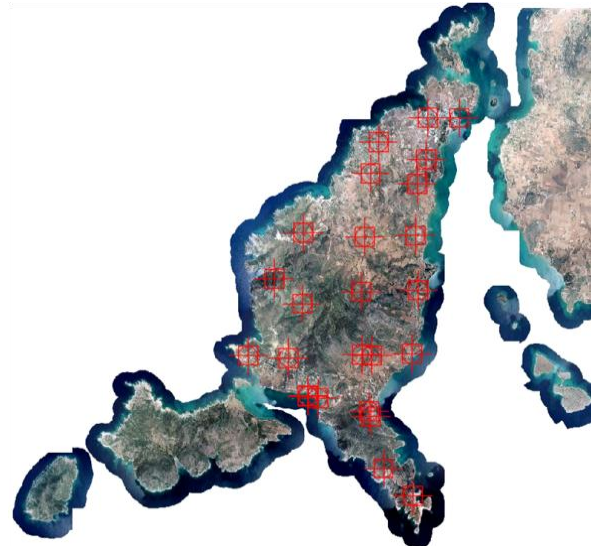


Figure 6. Checkpoints distribution on control dataset

4.2.4 Measurements - Results: 25 checkpoints were measured and used for the Pleiades 1B dataset and 26 checkpoints were used for the GeoEye-1 and LSO data scattered into areas with different terrain relief and land cover (Figure 5).

A/A	VLSO (Control Dataset)		PLEIADES B1		GEOEYE 1		LSO	
	X(m)	Y(m)	dX(m)	dY(m)	dX(m)	dY(m)	dX(m)	dY(m)
1	596781,77	4100183,44	-0,69	-0,28	-0,56	1,12	0,24	0,47
2	595845,18	4100188,57	-0,73	-0,02	-0,02	0,89	-0,39	0,35
3	595813,14	4098975,40	-0,05	-0,17	-0,18	1,24	0,29	0,40
4	594419,04	4099474,79	0,51	-0,09	-0,24	0,46	0,52	1,09
5	595546,93	4098254,51	-0,37	0,23	-0,24	0,79	0,84	0,86
6	594187,66	4098555,68	-0,23	-0,78	-0,34	0,08	-0,19	-0,10
7	595494,50	4096742,60	-0,45	0,49	-0,58	1,07	-0,29	0,87
8	595406,89	4096729,21	-0,28	-0,04	0,58	1,52	0,31	0,41
9	594027,42	4096706,90	-0,63	-0,70	0,28	0,27	0,11	0,26
10	592307,54	4096692,48	-0,09	-0,72	-0,14	1,00	-0,02	0,89
11	592229,01	4096831,51	-0,50	-0,68	0,00	1,07	0,16	0,81
12	595570,94	4095148,65	-0,65	0,15	-0,11	-0,91	-0,57	1,12
13	593924,05	4095109,99	0,39	-0,51	-0,66	0,33	-0,36	0,91
14	592201,41	4094754,63	-0,38	0,04	-0,44	0,73	-0,19	0,57
15	591581,53	4095387,22	-0,51	-0,6	-0,35	0,78	-0,39	0,64
16	591386,71	4095474,95	0,47	-0,14	0,86	1,04	0,02	0,74
17	595389,69	4093290,39	-	-	0,08	-1,31	-0,36	0,07
18	593939,63	4093262,95	0,69	-0,56	0,73	0,01	-0,55	0,16
19	591828,22	4093270,46	-0,77	-0,55	-1,48	-0,46	-0,68	-0,20
20	591811,63	4093172,45	-0,51	-0,2	-0,57	0,41	-0,40	0,20
21	590625,15	4093229,84	0,18	-0,91	-0,37	0,95	-0,45	0,70
22	592663,35	4091993,05	0,11	0,26	-0,22	0,71	-0,14	0,54
23	592370,47	4092052,04	0,09	0,49	-0,13	0,98	-0,12	0,36
24	592357,15	4092062,40	0,22	0,04	-0,08	0,68	-0,71	0,47
25	594197,98	4091451,92	-0,28	-0,28	-0,27	0,18	-0,06	-0,34
26	595326,84	4089050,41	-0,16	0,61	-0,44	0,29	-0,05	0,04

Table 1. Measured coordinates for GeoEye-1 and Pleiades 1B orthoimagery.

The differences dX,Y, are computed as $dX, Y = X, Y_{data} - X, Y_{check}$

It is noted that for Pleiades 1B was determined 1 checkpoint less due to the clouds over the area of the point. The coordinates of these checkpoints were determined on the control dataset, the aerial imagery orthomosaic (VLISO) provided from Hellenic National Cadastre & Mapping Agency S.A. (NCMA S.A) (0.25m GSD). In Table 1 are presented the measured coordinates of the checkpoints on the control dataset and the differences between those and the measured coordinates in the test datasets.

The results are presented with a statistical analysis and they are evaluated in order to present the merits and demerits of the imaging sensors involved. To this direction the Standard Deviation (σ) or sigma are computed as an indicator of how well the measurements fit each other and a measure of precision. In addition, the Root Mean Squares Error (RMSE) is computed for Northing and Easting coordinates. It is assumed that errors in the spatial data have random behavior and that systematic errors have been eliminated as best as possible

$$StDEV = \sqrt{\sum \frac{d^2}{n-1}} \quad (1)$$

$$RMSE_X = \sqrt{\sum_{i=1}^n (X_{data} - X_{check})^2} \quad (2)$$

$$RMSE_Y = \sqrt{\sum_{i=1}^n (Y_{data} - Y_{check})^2} \quad (3)$$

$$RMSE_{XY} = \sqrt{(RMSE_X)^2 + (RMSE_Y)^2} \quad (4)$$

where d = the deviation
 n = the number of check points
 X, Y_{check} = the check points coordinates measured on control dataset and
 X, Y_{data} = the points coordinates measured on test dataset

	RESIDUALS		
	ΔX		
	Pleiades B1	Geoeye-1	LSO
Chck Pts	25	26	26
StDEV(m)	0.374	0.388	0.467
RMSE _X (m)	0.389	0.607	0.495
	ΔY		
	Pleiades B1	Geoeye-1	LSO
	Check Pts	25	26
StDEV (m)	0.658	0.415	0.423
RMSE _Y (m)	0.838	0.453	0.465

Table 2. Resulting residuals of the measured checkpoints

As observed, in aerial imagery LSO and Geoeye-1 orthomosaic, the Standard Deviation and RMSE_{X,Y} differ indicating a systematic error in Y axis. Thus, a bias removal procedure was applied in order to evaluate orthoimages objectively and accurately.

The BIAS is estimated by the formula:

$$BIAS = \sqrt{RMSE_{XY}^2 - \sigma^2} \quad (5)$$

where σ = is the random error

Data Src	Pleiades B1		Geoeye-1		LSO	
RMS _{X,Y} - stdev	0,038	0,042	0,028	0,179	0,016	0,219
Linear Bias	0,181	0,193	0,164	0,518	0,110	0,467
Circular Bias	0,265		0,543		0,479	

Table 3. Bias calculations

	Pleiades B1	Geoeye-1	LSO
RMSE _X (m)	0.522	0.381	0.578
RMSE _Y (m)	0.646	0.453	0.465
Horizontal RESIDUALS			
	Pleiades B1	Geoeye-1	LSO
RMSE _{XY} (m)	0.646	0.866	0.649

Table 4. RMSEs and horizontal residuals after bias removal

Geoeye-1 data have the bigger RMSE_{XY} possibly due to bad image quality leading to erroneous GCPs measurements on the images. Pleiades 1B orthoimage has almost the same external accuracy as the orthomosaic from aerial imagery (LSO from NCMA S.A).

5. CONCLUSION

The main aim of this paper was to assess the geometric and radiometric quality of orthorectified high resolution satellite imagery from Pleiades-1B satellites through a comparative evaluation of their quantitative and qualitative properties. In addition, the advantages and limits of the Pleiades Imaging for producing Large Scale Orthophotos (LSO) are investigated. The visual assessment of the orthoimagery revealed that Pleiades 1B orthoimagery is especially promising presenting much more information and clearer forms. On the contrary, abrupt changes of brightness and contrast and high radiometric saturation levels were observed on the GeoEye-1 orthomosaic. The geometric evaluation reveals that the used LSO and Geoeye-1 orthomosaic suffer from a systematic error in Y axis. In addition, Pleiades 1B and LSO imagery have almost the same external accuracy.

Both radiometric and accuracy test results show that Pleiades 1B orthoimage has almost the same absolute accuracy as the orthomosaic from aerial imagery (LSO from Hellenic National Cadastre & Mapping Agency S.A.). Hence, it could easily replace aerial imagery, when it comes to orthoimage production. Furthermore, all data are adequate for producing LSO for mapping and GIS, according to JRC and NSSDA accuracy standards. The results also serve for a critical approach for the usability and cost efficiency of satellite imagery for the production of LSO.

ACKNOWLEDGEMENTS

The research leading to these results has been supported by European Union funds and National funds (GSRT) from Greece and EU under the project JASON: Joint synergistic and integrated use of eArth obServation, navigatiOn and commuNication technologies for enhanced border security funded under the cooperation framework. The authors would also like to thank Astrium GEO-Information Services which provided the Pléiades triplet for research and investigation purposes. Finally, the contribution of NCMA S.A, through the provision of the orthophoto and DEM, produced by aerial photography is acknowledged.

REFERENCES

Aguilar, M. A., Agüera, F., Aguilar, F. J., and Carvajal, F., 2008. Geometric accuracy assessment of the orthorectification

- process from very high resolution satellite imagery for Common Agricultural Policy purposes. *International journal of remote sensing*, 29(24), pp. 7181-7197.
- Astrium, 2012. *Pléiades Imagery User Guide*. October 2012-v2.0.
- Chavez, P. and Bowell, J., 1988. "Comparison of the spectral information content of Landsat thematic mapper and spot for three different sites in the Phoenix, Arizona region," *Photogramm. Eng. Remote Sens.*, vol. 54, no. 12, pp. 1699-1708.
- Cheng, Ph., Chaapel, C., 2008. Using WorldView-1 stereo data with or without ground control points. *GEOinformatics* 11 (7), pp. 34–39.
- Crespi, M., and De Vendictis, L., 2009. A procedure for high resolution satellite imagery quality assessment. *Sensors*, 9(5), pp. 3289-3313.
- Edwards, K. and Davis, P., 1994. The use of intensity-hue-saturation transformation for producing color shaded relief images. *Photogramm. Eng. Remote Sens.*, vol. 60, no. 11, pp. 1369–1373.
- Eisenbeiss, H., Baltsavias, E., Pateraki, M., and Zhang, L., 2004. Potential of IKONOS and QUICKBIRD imagery for accurate 3D-Point positioning, orthoimage and DSM generation. *International Archives of the Photogrammetry, Remote Sensing and Spatial Information Sciences*, 35(B3), pp. 522-528.
- FGDC. 1998. Geospatial Positioning Accuracy Standards Part 3: National Standard for Spatial Data Accuracy, FGDC-STD-007.3-1998 https://www.fgdc.gov/standards/projects/FGDC-standards-projects/accuracy/part3/index_html
- Gleyzes, M. A., Perret, L., and Kubik, P., 2012. Pleiades system architecture and main performances. *International Archives of the Photogrammetry, Remote Sensing and Spatial Information Sciences*, 39, B1.
- Gonzalez, R. C., and Woods, R. E., 2002. *Digital image processing*, 2nd. SL: Prentice Hall, 2.
- Greenfeld, J., 2001. Evaluating the accuracy of Digital Orthophoto Quadrangles (DOQ) in the context of parcel-based GIS. *Photogrammetric engineering and remote sensing*, 67(2), pp. 199-206.
- Haydn, R., Dalke, G. W., Henkel, J., and Bare, J. E., 1982. Application of the IHS color transform to the processing of multisensor data and image enhancement. In *Proceedings of the International Symposium on Remote Sensing of Environment, First Thematic Conference: "Remote sensing of arid and semi-arid lands"*, Cairo, Egypt.
- Helder, D., Choi, J., 2003. On-orbit Modulation Transfer Function (MTF) measurements on QuickBird. In: *Proceedings of the 2003 High Spatial Resolution Commercial Imagery Workshop*, NASA/NIMA/USGS Joint Agency Commercial Imagery Evaluation Team: Reston, VA, USA.
- Ioannidis, C., and Katsigiannis, A., 2006. Accuracy comparison tests on ortho-rectified high resolution satellite images. *Revue française de photogrammétrie et de télédétection*, (184), 95-100.
- Ioannou, M. T., and Georgopoulos, A., 2013. Evaluating large scale orthophotos derived from high resolution satellite imagery. In *First International Conference on Remote Sensing and Geoinformation of Environment*. International Society for Optics and Photonics, pp. 879515-879515.
- Jacobsen, K., 2011. Characteristics of very high resolution optical satellites for topographic mapping. *International Archives of the Photogrammetry, Remote Sensing and Spatial Information Sciences*, XXXVIII (4/W19), on CDROM.
- Kapnias, D., Milenov, P., and Kay, S. 2008. Guidelines for Best practice and quality checking of ortho imagery. *Joint Research Centre*, (3.0).
- Kohm, K., 2004. Modulation transfer function measurement method and results for the OrbView-3 high resolution imaging satellite. *International Archives of the Photogrammetry, Remote Sensing and Spatial Information Sciences*, 35 (B1), pp. 7–12.
- Leger, D., Viallefont, F., Deliot, P., Valorge, C., 2004. On-orbit MTF assessment of satellite cameras. In: Morain, S.A., Budge, A.M. (Eds.), *Post-Launch Calibration of Satellite Sensors*. Taylor and Francis Group, London, UK, pp. 67–76.
- Niu, X., Wang, J., Di, K., Lee, J.-D., Li R., 2004. Geometric modelling and photogrammetric processing of high-resolution satellite imagery. In: *The International Archives of the Photogrammetry, Remote Sensing and Spatial Information Sciences*, Istanbul, Turkey, Vol. XXXV, Part B4, pp. 689-694.
- Padwick, C., Deskevich, M. I. C. H. A. E. L., Pacifici, F., and Smallwood, S., 2010. WorldView-2 pan-sharpening. *Proc. American Society for Photogrammetry and Remote Sensing*, 13.
- Palsson, F., Sveinsson, J. R., Benediktsson, J. A., and Aanaes, H., 2012. Classification of pansharpened urban satellite images. Selected Topics in Applied Earth Observations and Remote Sensing, *IEEE Journal of*, 5(1), pp. 281-297.
- Poli, D., Remondino, F., Angiuli, E., and Agugiaro, G., 2014. Radiometric and geometric evaluation of GeoEye-1, WorldView-2 and Pléiades-1A stereo images for 3D information extraction. *ISPRS Journal of Photogrammetry and Remote Sensing*.
- Tu, T. M., Huang, P. S., Hung, C. L., and Chang, C. P., 2004. A fast intensity-hue-saturation fusion technique with spectral adjustment for IKONOS imagery. *Geoscience and Remote Sensing Letters, IEEE*, 1(4), pp. 309-312.
- Carper, W. J., Lillesand, T. M., and Kiefer, P. W., The use of intensity-hue-saturation transformations for merging spot panchromatic and multispectral image data, *Photogramm. Eng. Remote Sens.*, vol. 56, no. 4, pp. 459–467.
- Zhou, G., Li, R., 2000. Accuracy evaluation of ground points from IKONOS high-resolution satellite imagery. *Photogrammetric Engineering and Remote Sensing*, 66(9), pp. 1103-1112.